ABSTRACT

Title of dissertation: SIGNAL DENOISING FOR EXO-200
AND AN IMPROVED LIMIT ON
NEUTRINOLESS DOUBLE-BETA DECAY

Clayton G. Davis, Doctor of Philosophy, 2014

Dissertation directed by: Professor Carter Hall
Department of Physics

The EXO-200 detector is designed to measure the spectrum of Xenon-136 double-beta ($\beta\beta$) decay. This extremely low-rate radioactive process is interesting on its own, but more profound is its potential to reveal non-standard neutrinoless double-beta ($\beta\beta0\nu$) decay. $\beta\beta0\nu$ decay, if it occurs, would have important consequences for our understanding of the neutrino sector of the standard model. It would demonstrate the type of the neutrino mass term; set the mass scale of the neutrino sector; and demonstrate the first direct observation of lepton number non-conservation.

In the EXO-200 detector, we measure the summed energy of the two emitted electrons. The summed-electron-energy spectrum of standard $\beta\beta$ decay produces a smooth spectrum due to the "missing" energy of the two emitted neutrinos. In contrast, the non-standard $\beta\beta0\nu$ decay has no neutrino products, and emits energy only in the form of electrons. Since all energy is captured by the electrons, the sum of electron energies will always be 2458 keV; thus, we can discover this process by looking for a peak in the summed electron energy spectrum at this energy.

The sensitivity of the search depends on two basic factors: accumulated Xenon-136 exposure, and expected background near 2458 keV from non-$\beta\beta0\nu$ decays. The EXO-200 detector was designed to minimize background primarily through its construction. All materials used in the construction of the EXO-200 detector were carefully screened for low concentration of radioactive backgrounds, making the EXO-200 detector one of the lowest-background detectors in the world.

Backgrounds were also minimized in EXO-200 by ensuring that the energy resolution of the detector would be excellent. Good energy resolution ensures that all monoenergetic peaks (including both $\beta\beta0\nu$ and background gamma lines) will be sharp. When background is integrated over the width of the $\beta\beta0\nu$ expected peak, we wish for the integrated number of expected counts to be as small as possible; when peaks are sharper, we can expect that integral to be smaller.

When the EXO-200 detector turned on, its scintillation signals observed more electronic noise than had been expected based on design goals. The present work is concerned with improving the energy resolution of the EXO-200 detector by removing electronic noise by an offline denoising process. It will be concerned with a detailed characterization of the signal and noise behavior of the EXO-200 scintillation measurements; a novel algorithm for denoising such signals; and results from denoised EXO-200 data will be presented, showing an improved $\beta\beta0\nu$ limit in Xenon-136. Since this scheme is still in its infancy, possible future improvements will be described throughout, along with discussion of motivations for these improvements.

SIGNAL DENOISING FOR EXO-200 AND AN IMPROVED LIMIT ON NEUTRINOLESS DOUBLE-BETA DECAY

by

Clayton G. Davis

Dissertation submitted to the Faculty of the Graduate School of the
University of Maryland, College Park in partial fulfillment
of the requirements for the degree of
Doctor of Philosophy
2014

Advisory Committee:
Professor Carter Hall, Chair/Advisor
Professor Radu Balan
Professor Betsy Beise
Professor Rabindra Mohapatra
Professor Peter Shawhan

Preface

If needed.

Foreword

If needed.

Dedication

If needed.

Acknowledgments

Thanks all for lots of help...

Contents

List of Figures

List of Abbreviations

EXO	Enriched Xenon Observatory (family of current or planned detectors)
EXO-200	Current (200-kg) iteration of the EXO family of detectors
nEXO	Planned next-generation EXO detector
APD	Avalanche Photo-diode
ADC	Analog-Digital Converter, or one of its discrete output units
DAQ	Data Acquisition System

Chapter 1: Theory of $\beta\beta 0\nu$ Decay

Standard-model $\beta\beta$ decay is the result of the particle interaction $2d \rightarrow 2u + 2e^- + 2\bar{\nu}_e$ mediated by W^--exchange, as depicted in Figure 1.1. It is effectively the simultaneous occurance of two β decays from the same nucleus.

$\beta\beta$ decay is the result of a second-order weak interaction, so it has a remarkably long half-life; however, it does not violate any symmetries and is, in this sense, a mundane prediction of the Standard Model. Although many nuclei are expected to decay by $\beta\beta$, the process is thoroughly masked by conventional β decay in most of them. There are, however, isotopes which are forbidden from undergoing β decay by energy conservation, yet permitted to undergo $\beta\beta$ decay. These are in all known instances isotopes with even-even proton-neutron numbers; β decay would take these isotopes to odd-odd, which is energetically disfavored due to the loss of pairing forces between like nuclei, while $\beta\beta$ decay permits these isotopes to remain in a favorable even-even state. Isotopes which follow this pattern are considered $\beta\beta$ candidates.

The detection and study of $\beta\beta$ decay provides an opportunity to test a new class of nuclear matrix computations, and also a chance for experimentalists to push the boundaries of low-background experiments; however, the primary appeal
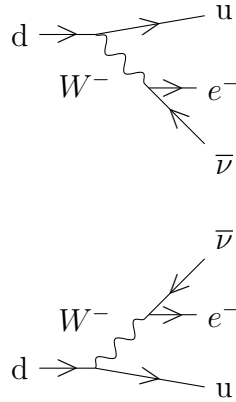
Figure 1.1: Feynman diagram for $\beta\beta2\nu$ decay. The reaction products are equivalent to two β decays in succession, but this reaction can occur even if a single β decay would be energetically forbidden.
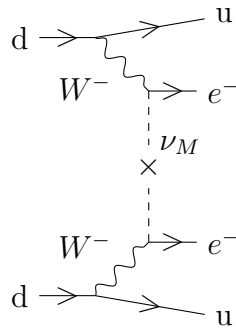
Figure 1.2: Feynman diagram for $\beta\beta0\nu$ decay. A virtual neutrino mediates the exchange. This is only possible if $\bar{\nu}_R$ can oscillate to ν_L, and the interaction that induces this oscillation also generates neutrino mass.

of $\beta\beta$ decay is through the opportunity it provides to probe the nature of neutrinos. It has been suggested as early as 1937 that neutrinos could possess mass through a novel neutrino-antineutrino interaction, provided that the neutrino be its own antiparticle [23]. As evidence mounted through the 1990's that neutrinos must have nonzero mass (see, in particular, the observation of neutrino oscillation in [15]), interest in possible mass-generating mechanisms has increased – including Majorana's mechanism.

If neutrinos do have Majorana mass interactions, then any isotope that undergoes $\beta\beta$ decay can also undergo the related process $2d \rightarrow 2u + 2e^-$, depicted in Figure 1.2, in which the two outgoing neutrinos in $\beta\beta$ decay are replaced by one virtual neutrino. This is only possible if neutrinos are their own antiparticles because the timelike arrow of the neutrino cannot be specified. We refer to the standard process as $\beta\beta2\nu$ decay and the novel process as $\beta\beta0\nu$ decay.

A clear observation of $\beta\beta0\nu$ would immediately yield a number of interesting physical insights. The existence of the process automatically demonstrates non-conservation of total lepton number, since the lepton number increases by 2. Numerous theories have suggested that lepton number may not be conserved [14][6], but none have yet reported a positive result. In the conventional Standard Model with massless neutrinos, lepton number conservation is an accidental symmetry [16], but since neutrinos are known to have mass, there is no longer *a priori* any reason to expect conservation or non-conservation.

A second conclusion, as discussed above, would be that neutrino mass comes from a Majorana mass term. This term appears in the lagrangian (for each mass
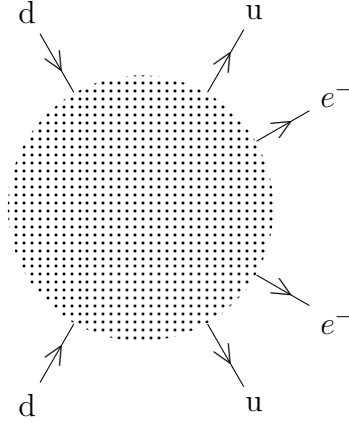
Figure 1.3: A generic $\beta\beta0\nu$ process, with no assumptions of the underlying mechanism. If $\beta\beta0\nu$ is observed, it requires that this reaction is possible even though it does not strictly imply that the oscillation in Figure 1.2 is the cause.

eigenstate) as

$$\begin{aligned}
\mathcal{L}_{Maj} &= -\frac{m_L}{2}\left(\overline{\Psi_L^c}\Psi_L + \overline{\Psi_L}\Psi_L^c\right) \\
&\quad -\frac{m_R}{2}\left(\overline{\Psi_R^c}\Psi_R + \overline{\Psi_R}\Psi_R^c\right),
\end{aligned}$$

where the superscript-c represents charge conjugation. (This is the reason that Majorana mass terms are only possible for a chargeless lepton.) The masses m_L and m_R may be tuned independently; since there has never been an observation of right-handed neutrinos or left-handed anti-neutrinos, it is possible that $m_R = 0$ and that the fields Ψ_R and Ψ_R^c do not exist in nature [13].

It is worth noting that the interaction term above assumes no mediating particles in the mechanism. However, if $\beta\beta0\nu$ decay is observed, it leads very generally to a conclusion that neutrinos have an *effective* Majorana mass interaction [25]. We can see this by examining the generic diagram for $\beta\beta0\nu$ decay in Figure 1.3. No
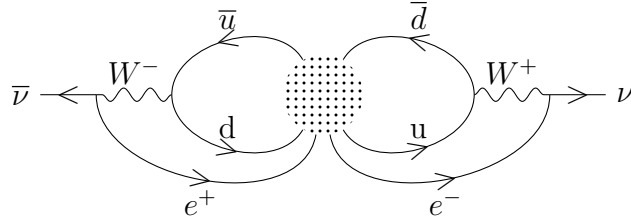
Figure 1.4: Since $\beta\beta0\nu$ requires that the reaction in Figure 1.3 occurs, we can insert that diagram into this larger one and assert that regardless of the underlying mechanism, $\beta\beta0\nu$ implies an effective neutrino mass generated by $\overline{\nu}$-ν oscillation as a higher-order process.

matter what the mechanism of the decay is, we can insert this diagram into the larger one in Figure 1.4 and see that an effective neutrino-antineutrino mass vertex is implied by the existence of $\beta\beta0\nu$ decay.

If the mechanism of $\beta\beta0\nu$ decay really is, at tree level, a neutrino mass term as shown in Figure 1.2, then it is possible to infer the mass scale of the neutrino from the observed rate of decay. To lowest order we can assert that

$$[T_{1/2}^{0\nu}]^{-1} \propto \langle m_{\beta\beta}\rangle^2 = \left|\Sigma_k m_k U_{ek}^2\right|^2,$$

where U_{ek} is the neutrino mixing matrix and the m_k identify the three neutrino mass eigenstates. The constant of proportionality is isotope-dependent; state-of-the-art nuclear matrix computations can provide it within a factor of $2-3$ [1]. We will not consider the complex challenges of these computations here.

There are bounds on the values that may be seen, based on previous results in $\beta\beta0\nu$ decay and other measurements. Figure 1.5 shows how the various mass parameters can be related to each other. M, the combined masses of all three
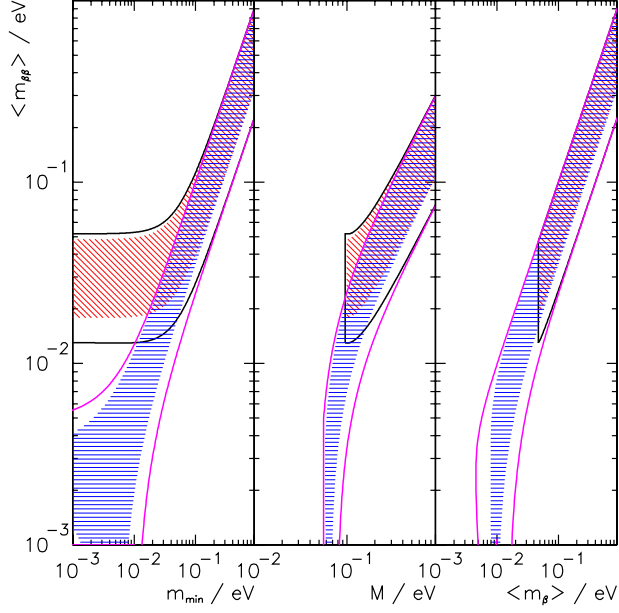
Figure 1.5: The fundamental parameters m_1, m_2, m_3 of the three neutrino mass eigenstates are not directly measured; instead, experiments give different weighted sums of the three that allow these parameters to be constrained. M is the sum of the three mass values; $\langle m_\beta \rangle$ is the effective mass relevant to β decay, and $\langle m_{\beta\beta} \rangle$ is the effective mass probed by $\beta\beta 0\nu$ decay. The plots above indicate the relation, in the case of Majorana neutrinos, among these various parameters based on our current knowledge of Δm^2 and mixing angles (red lines if the smaller Δm^2 belongs to the lighter neutrinos, black lines if it belongs to the heavier neutrinos) and if these parameters were known exactly (hatched areas). Image provided by [13].

neutrino flavors, can be limited by cosmological observations; recent results from Planck combined with WMAP and baryon acoustic oscillations have restricted $M < 0.23$ eV [5]. Measurements of the β decay spectrum of Tritium have yielded bounds on $\langle m_\beta \rangle$, the weighted average mass of the electron-neutrino; this parameter is currently known to be less than 2.5 eV [12], and the KATRIN experiment is expected to begin data-taking in 2012 with a sensitivity down to 0.2 eV [4].

The strongest limits on $\langle m_{\beta\beta} \rangle$ have been published by the Heidelberg-Moscow experiment studying ^{76}Ge. The results of this experiment have been interpreted in conflicting ways by its collaboration: the faction that asserts a positive detection of $\beta\beta0\nu$ has most recently published a value of $\langle m_{\beta\beta} \rangle = 0.32 \pm 0.03$ eV [22], while the full collaboration's strongest limit was $\langle m_{\beta\beta} \rangle < 0.35$ eV (both neglecting uncertainty in the nuclear matrix elements) [9]. In addition to the disagreement within the Heidelberg-Moscow collaboration, though, there is also widespread agreement that it is unreliable to draw conclusions on $\langle m_{\beta\beta} \rangle$ from only one isotope due to the poorly-understood uncertainties in the nuclear matrix elements [1]. All of this means that there is significant interest by many collaborations, working with many different isotopes in parallel, to probe below the threshold set by the Heidelberg-Moscow experiment to confirm or refute the claimed discovery.

Chapter 2:   The EXO-200 Detector

Among the experiments with potential to match the sensitivity of Heidelberg-Moscow is the Enriched Xenon Observatory (EXO). In particular, the EXO-200 detector is designed to hold 200 kg of Xe enriched to 80% in ^{136}Xe, and anticipates probing down to $\langle m_{\beta\beta} \rangle \sim 0.1$ eV [19]. Xenon is a convenient material to study because it is a noble element, making it easy to purify chemically. It has no long-lived radioactive isotopes, so there is no concern of cosmogenic activation of the Xenon while aboveground. It has a fairly high Q-value of 2.458 MeV, giving it a larger phase-space for its decay products and putting its peak out of reach of many common backgrounds. Xenon also provides two means to measure energy from a decay: under the influence of an electric field, ionization charge in pure Xenon will drift; and regardless of electric field, excited Xenon scintillates. The ratio of scintillation to ionization depends on electric field and the density of the energy deposit; thus, at high enough electric field discrimination is possible between high-energy-density α-decay and lower-energy-density β- and γ-decay. Another benefit of Xenon is that, since it can act as an energy detector in its pure gaseous or liquid state, it is easy to make a large monolithic Xenon detector. We will here review how the EXO-200

HV FEEDTHROUGH
COPPER VESSEL
CATHODE
VUV TEFLON
REFLECTOR TILES
U AND V
WIRE PLANES

WELDED
BULKHEAD

Xe AND
CABLE DUCT

APD ARRAY

WIRING
SYSTEM

FIELD
SHAPING RINGS

10cm
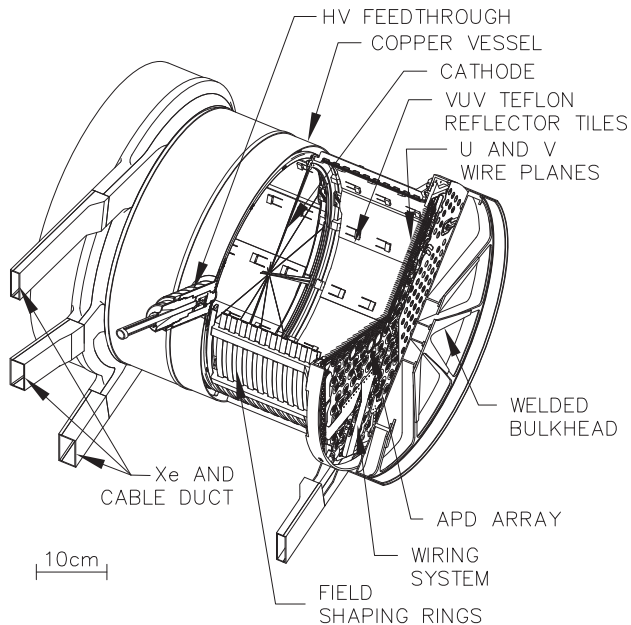
Figure 2.1: Schematic of the inner EXO-200 TPC.

experiment has been constructed to exploit these properties and explore down to interesting neutrino masses.

The core of the EXO-200 detector is a cylindrical time-projection chamber (TPC), depicted in Figure 2.1, under a potential of roughly 400 V/cm. The electric field is shaped to be parallel to the axis of the TPC throughout its fiducial volume. The cathode is located in the middle of the TPC, and charge is collected on grids of parallel wires on either end of the TPC, giving a high-quality probe of the total ionization charge and location along one axis. Also on both ends of the TPC, in front of these collection wires is another grid of parallel wires, orthogonal to the collection wires, which identifies an induced signal from passing ionization charge to give another position coordinate. Finally, on both endcaps of the TPC are many large-area avalanche photodiodes (LAAPDs) which can detect the scintillation light

9

from the primary decay [10]. The time difference between scintillation and charge collection gives a third position coordinate from a decay, and the scintillation also can give a secondary measurement of the energy of the deposit. As noted above, comparing the scintillation and collected ionization allows α-decays to be identified, removing one broad source of backgrounds.

The Xenon must be kept extremely pure, both to reduce backgrounds and to permit the ionization charges to drift farther with less attenuation. To accomplish this, the detector has two pipes feeding into it so that Xenon may be circulated out of the detector continuously for repurification. This is done using SAES Zirconium getters, which filter out all chemically reactive elements and return only noble elements. Radioactive isotopes which are not filtered out are ^{85}Kr (which has a Q-value much lower than that of ^{136}Xe, making it fairly harmless) and all forms of Radon (some of whose daughter products can deposit energy around the Q-value of ^{136}Xe).

The TPC itself is made of oxygen-free high-thermal-conductivity (OFHC) copper that was kept under concrete shielding during its time aboveground to protect it from neutron-induced activation. Nevertheless, the copper may be a significant source of backgrounds in the energy range of interest, primarily due to natural contamination by ^{40}K, ^{238}U and ^{232}Th [8]. To mitigate this, significant effort has been expended in making the copper walls as thin as possible, averaging 1.5 mm thick. The ductility of copper makes such thin walls technically challenging, and a significant infrastructure has been developed to maintain the pressure of ultrapure HFE coolant, in which the TPC is immersed, so that the pressure difference can be controlled to ~ 10 torr.

Other significant sources of background may be the charge collection wires that pass through the TPC and the LAAPDs on its ends. Both backgrounds have been minimized by limiting the total mass and carefully selecting materials to use. The charge collection wires are photo-etched from phosphor bronze; the etching process was found to contribute to surface contamination, which was minimized by the use of clean etching agents and the use of a more aggressive cleaning procedure after etching [8]. The LAAPDs are designed to minimize the radioactive contamination they introduce. They were designed without standard ceramic encapsulation; instead the LXe is itself relied upon to insulate them. Additionally, Aluminum used in the LAAPDs was found to be high-background, and was replaced with an acceptable substitute. These efforts have reduced the activity introduced by the LAAPDs [8][10].

These are a few of the critical subsystems that were screened prior to use. More details will be presented in a forthcoming detector paper to be written by the EXO collaboration.

Chapter 3: Denoising Theory

As has been discussed, the performance of double-beta experiments like EXO-200 is partially determined by their energy resolution. In EXO-200, the energy resolution is limited by the scintillation energy resolution, which in turn is dominated by electronic noise in the APDs. Significant effort must therefore be expended to understand and reduce the noise in the scintillation signals.

When the noise in the APDs is studied, it was found that the individual APD channels met targetted root-mean-square noise levels of 2000 electrons. However, rather than observing the noise on summed APD channels increase proportionally to the square root of the number of channels, the summed APD noise is roughly two to three times higher than projected. This worse-than-expected scaling of the noise with channels indicates that noise across different channels is correlated, and further analysis confirms that the bulk of the noise on an unshaped APD waveform is correlated with other channels, as shown in Figure 3.1. There are many possible sources of coherent noise in the hardware, and reducing the amount of coherent noise is a topic for further research. [27]

However, the observation that coherent noise is the dominant source of noise in
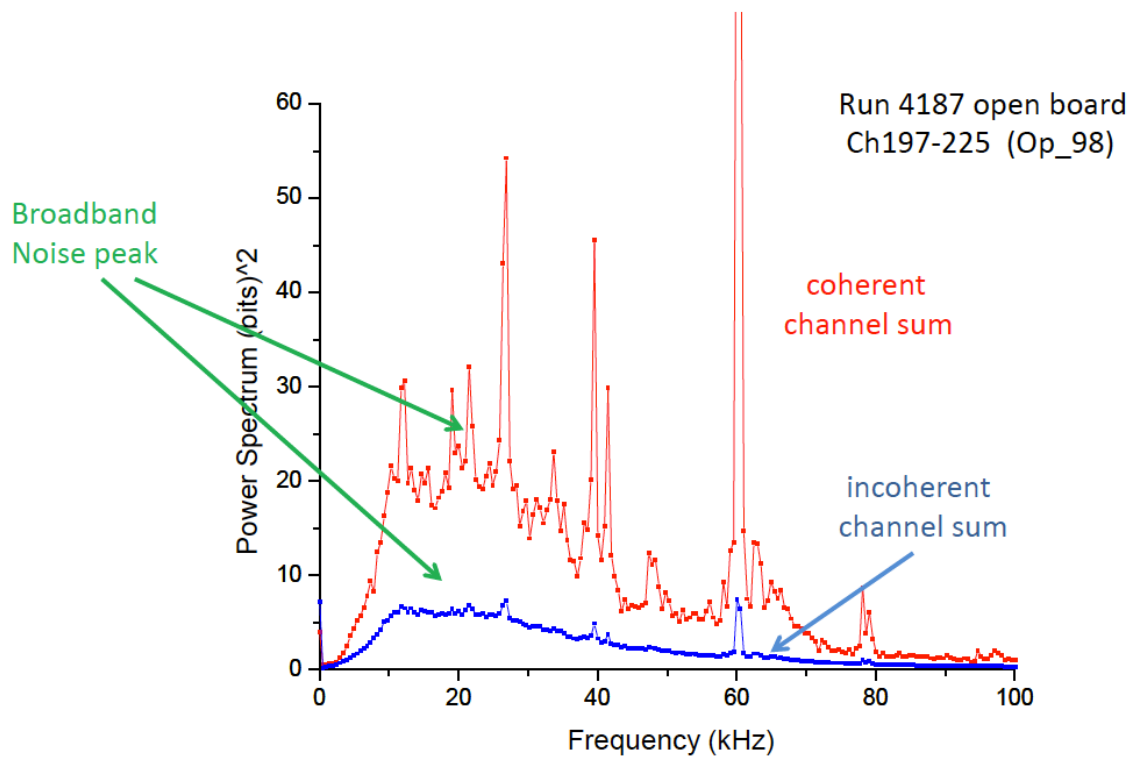
Figure 3.1: Coherent and incoherent noise power spectra for a sample set of APD channels without signal shaping. [27]

the APDs, and thus also the limiting factor in EXO-200's energy resolution, means that it should be possible to exploit these correlations and reduce the level of noise in offline analysis. This chapter will describe a scheme to accomplish that goal and produce an optimal estimate of scintillation energy which takes noise correlations into account.

It is worth noting that in fact there are a number of different qualitative approaches to reducing the noise levels in the scintillation channel. In casual terms, we will refer to "passive" approaches as those in which components of our signals are weighted more or less heavily based on their relative signal-to-noise content. "Active" approaches, by contrast, will be classified as those which attempt to improve the signal-to-noise content of signal components. We have identified the following three types of denoising:

Frequency weighting

On a given channel signal, weight more heavily the frequency components which contain larger signal-to-noise ratio. This passive denoising scheme requires knowledge of the shapes in fourier space of a signal and the power spectrum of the noise.

Channel weighting

Different channels may have different levels of noise, so some may generally have higher-quality signals. More importantly, though, the amount of signal on a given channel depends strongly on the proximity of the APD gang to the source of scintillation within the detector. This passive denoising scheme

therefore allows us to weight more heavily the channels which have more scintillation, provided we can identify these weights on an event-by-event basis. This requires knowledge of the magnitude of noise on each channel and of the correspondence between event position and signal magnitude on each APD gang; the latter is described by the lightmap, described earlier.

Noise subtraction

This active form of denoising consists of using correlations between noise on different channels to produce a better estimate of the noise component of signals than each signal taken independently could provide. To accomplish this, we will require detailed information about the pairwise noise correlations across channels at each frequency.

In the following, we will describe a general linear operator on the APD signals which in principle can accomplish each of these forms of denoising, and we will presume that all of the described inputs are available; by identifying the parameters for that linear operator which are optimal, we can be confident that the denoising operator we produce will accomplish all three forms of denoising described above.

3.1   Setup

We first establish a number of notational conventions:

- i, j will represent indices over APD channels.

- a, b, c will represent indices of signals in an event.

- τ will represent the time indices of a discrete waveform; t_a represents the calendar time of a signal a.

- f, g will represent the frequency indices of Fourier-transformed waveforms.

- For a waveform $*[\tau]$, we will represent the discrete Fourier transform of that waveform with $\widetilde{*}[f]$, where the particular convention used to evaluate the Fourier transform is not significant.

- For a Fourier-transformed waveform $\widetilde{*}[f]$, we denote the real and imaginary parts of that waveform by $\widetilde{*}^R[f]$ and $\widetilde{*}^I[f]$, respectively.

- For an unknown parameter $*$, the symbol $\widehat{*}$ will identify an estimator for $*$.

- For an expression $*$ containing random variables, $\langle * \rangle$ is the expectation value of $*$.

We describe the data as a collection of discretely sampled waveforms, $X_i[\tau]$. We assume that all signal times and shapes are already known, so we can model the waveforms by $X_i[\tau] = \sum_a M_{ia} Y_{ia}[\tau] + N_i[\tau] + b_i$, where Y is the shape of signal a on channel i, M is the magnitude of that signal, and N and b represent the electronic noise and baseline, respectively, of the channel.

To break the degeneracy between M and Y, we choose to fix the magnitude of the template signal Y. We choose to require that the signal Y has a magnitude of one, as described in figure 3.2. We assume that the expected magnitude of a signal on channel i from a single-site 2615-keV deposit is known, and is characterized as a function $L_i(\vec{x}, t)$ of the deposit position $\vec{x}$ and calendar time t. The exact methods

16

for measuring $L_i(\vec{x}, t)$ will be described in chapter 5. In cases where a multi-site event deposits energy in multiple locations, we will use the charge information to estimate the energy deposited in each location; the estimated lightmap yield from such an event will be a weighted sum:

$$L_i^{MS}(\vec{x}_1, \ldots, \vec{x}_{n_{max}}, t) = \frac{\sum_n E_n^{charge} L_i(\vec{x}_n, t)}{\sum_n E_n^{charge}}. \tag{3.1}$$

For notational simplicity, we will still characterize the expected yield on a gang i from a multi-site event as $L_i(\vec{x}, t)$; in practice it will always be clear how to compute the expected yields for any event from this function. We can thereby characterize the expected yields M_{ia} from an event with energy E_a as:

$$\langle M_{ia} \rangle = L_i(\vec{x}_a, t_a) E_a. \tag{3.2}$$

Noise correlations will be much simpler in frequency space, so we take the Fourier transform and drop the zero-frequency component to obtain

$$\widetilde{X}_i[f] = \sum_a M_{ia} \widetilde{Y}_{ia}[f] + \widetilde{N}_i[f]. \tag{3.3}$$

As with the lightmap, we will assume that all correlations in the noise, of the form

$$\left\langle \widetilde{N}_i^R[f] \widetilde{N}_j^R[g] \right\rangle \left\langle \widetilde{N}_i^R[f] \widetilde{N}_j^I[g] \right\rangle$$
$$\left\langle \widetilde{N}_i^I[f] \widetilde{N}_j^R[g] \right\rangle \left\langle \widetilde{N}_i^I[f] \widetilde{N}_j^I[g] \right\rangle, \tag{3.4}$$

are known; our means of measuring these correlations will be described in chapter 4.

3.2 The Signal Model

It is first important to characterize the response of the APDs to energy deposits in EXO-200. This will require us to understand the signal amplification of the detector
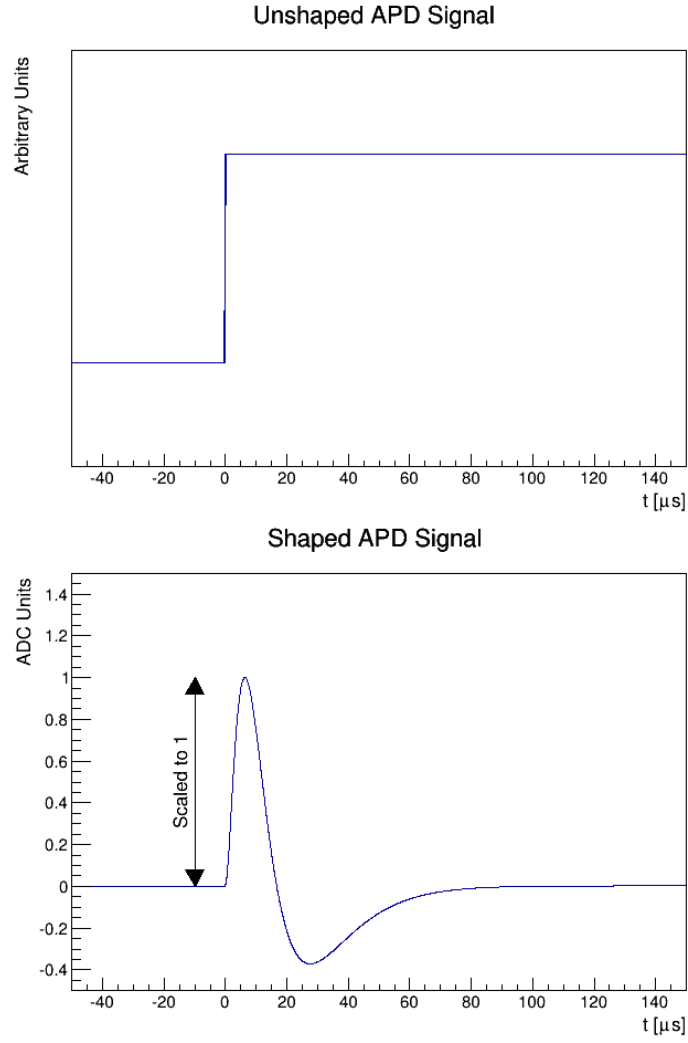
Figure 3.2: Shaped and unshaped APD waveforms. The normalization is shown to make the peak of the shaped waveform have a magnitude of one, and the time axis is shifted so that the unshaped waveform is a step function centered at $t = 0$.

at each physical stage, as well as the noise introduced by each of these processes. We will describe both in detail here.

3.2.1 APD Noise

We will assume that there are two sources of noise in this model. First, the electronic noise $N_i[\tau]$ is assumed to be random. We require that noise with different frequencies is uncorrelated:

$$\left\langle \widetilde{N}_i[f]\widetilde{N}_j[g] \right\rangle = 0 \text{ when } f \neq g.$$

The noise correlations $\left\langle \widetilde{N}_i[f]\widetilde{N}_j[f] \right\rangle$ are assumed to be known; our means for measuring them are described in chapter 4.

The second random variable will be the magnitude of the signal itself, M_{ia}. When an energetic decay occurs in bulk of the detector, it will release some number of photons. We will denote the number of photons released by signal a by $P_a^{(0)}$, and this is the parameter we wish to measure. However, the magnitude signal actually observed on APD channels number of photons actually collected by sensors is a random variable whose distribution depends on $P_a^{(0)}$, and we will now identify the chain of events which produce it.

First, each APD gang i has some number $P_{ia}^{(1)}$ of photons which reach them. The mean fraction of photons reaching a particular gang i from position $\vec{x}_a$, $f_i(\vec{x}_a)$, is assumed to be known; however, the initial paths of the optical photons emitted from the source, their trajectories through the Xenon, and their success in reflecting off of teflon are all random, so we treat $P_{ia}^{(1)}$ as a Poisson-distributed random variable

with mean $f_i(\vec{x}_a)P_a^{(0)}$. A typical deposit from a $\beta\beta0\nu$ event may deposit up to roughly 1000 photons on a nearby APD gang, resulting in roughly 3% uncertainty from photon statistics; in the bulk of the Xenon, it may be that the largest single APD signal is only one-tenth of this size, resulting in closer to 10% uncertainty due to photon statistics on the nearest APD gang. Thus, we find that the Poisson noise on a single APD channel may be quite significant.

Additionally, the number of photons reaching different gangs are not uncorrelated; since a photon which reaches gang i cannot deposit on a different gang j, $P_{ia}^{(1)}$ and $P_{ja}^{(1)}$ are anticorrelated for different gangs $i \neq j$. This process is described by a multinomial distribution. Explicitly, we can identify the expectation values of a multinomial distribution:

$$\left\langle P_{ia}^{(1)} \right\rangle = f_i(\vec{x}_a)P_a^{(0)} \tag{3.5}$$

$$\left\langle P_{ia}^{(1)} P_{jb}^{(1)} \right\rangle = \left\langle P_{ia}^{(1)} \right\rangle \left\langle P_{jb}^{(1)} \right\rangle + \left[f_i(\vec{x}_a)\delta_{ij} - f_i(\vec{x}_a)f_j(\vec{x}_a) \right] P_a^{(0)} \delta_{ab} \tag{3.6}$$

(As a detail, we should note that the multinomial distribution is an incorrect model in one important respect: photons may reflect off of teflon one or more times on its way to the APD. Photons incident on the teflon may be absorbed, leading to a reflection efficiency which may be less than one. Furthermore, it is possible that teflon may be mildly fluorescent at the wavelength of our scintillation, leading to an increase in efficiency for reflection. As a result, photons which reflect off of teflon experience a combination of variances from each path photons travel and variances in each gain which they undergo. These conditional variances will always be larger than a simple Poisson distribution would indicate [24], so our variance estimate for

$P^{(1)}$ is probably an underestimate.)

Following the random process associated with photons reaching the APD gangs, there is also randomness associated with signal amplification internally in the APDs. These processes are described in detail in [10], but we can summarize that:

1. Optical photons in the liquid xenon arrive at the active layer of the APDs have a wavelength of roughly 178 nm, meaning that each optical photon has an energy of roughly 7.0 eV. The energy required to produce one electron-hole pair in silicon is roughly 3.66 eV, which means that each incident photon produces roughly 1.9 electron-hole pairs; we will define $P_{ia}^{(2)}$ to be the number of electron-hole pairs actually produced from $P_{ia}^{(1)}$ incident photons. The corresponding Fano factor for electrons produced in silicon is roughly 0.1, meaning that in addition to the uncertainty in $P_{ia}^{(1)}$ which we have already characterized, there is an additional uncorrelated variance in $P_{ia}^{(2)}$ equal to $0.1 \left\langle P_{ia}^{(2)} \right\rangle$. The correlations in the parameters $P_{ia}^{(2)}$ are therefore:

$$\left\langle P_{ia}^{(2)} \right\rangle = 1.9 \cdot P_{ia}^{(1)} \tag{3.7}$$

$$\left\langle P_{ia}^{(2)} P_{jb}^{(2)} \right\rangle = (1.9)^2 \left\langle P_{ia}^{(1)} P_{jb}^{(1)} \right\rangle + 0.1 \left\langle P_{ia}^{(2)} \right\rangle \delta_{ij} \delta_{ab} \tag{3.8}$$

2. Electron-hole pairs are then amplified by an avalanche process inside the APDs. The magnitude of this gain is APD-dependent, generally on the order of $200 - 300$, and can be identified by a time-dependent quantity $G_i^P(t)$; we will call the number of output electrons $P_{ia}^{(3)}$. In addition to amplification of existing noise in $P_{ia}^{(2)}$, two additional source of noise are introduced. First,

there is statistical variance in the amplification experienced by each electron due to the randomness of the avalanche process. This variance is dependent on many factors, including the gain, and scales like the square root of the number of electrons; we define the variance on the gain experienced by a single electron as $\sigma^2_{G_i}(t)$. From [10], $\sigma^2_{G_i}(t)$ is approximately equal to $\left(G^P_i(t)\right)^2$ when $G^P_i(t) = 100$; as a result, we approximate $\sigma^2_{G_i}(t) \approx \left(G^P_i(t)\right)^2$. Second, there are gain non-uniformities in the diode volume, which contribute variance proportional to the square of the number of initial electron-hole pairs; we will identify the proportionality constant as σ^2_{NU}, which may depend on time and APD gang. The magnitude of this uncertainty is not well-known, but may be significant. Our current code base treats σ^2_{NU} as zero; however, future analyses will likely attempt to estimate it, and the derivation which follows will retain it as an aid to that anticipated work. The correlations in the parameters $P^{(3)}_{ia}$ are therefore:

$$\left\langle P^{(3)}_{ia} \right\rangle = G^P_i(t_a) P^{(2)}_{ia} \tag{3.9}$$

$$\left\langle P^{(3)}_{ia} P^{(3)}_{jb} \right\rangle = G^P_i(t_a) G^P_j(t_b) \left\langle P^{(2)}_{ia} P^{(2)}_{jb} \right\rangle + \left[P^{(2)}_{ia} \sigma^2_{G_i}(t_a) + \left(P^{(2)}_{ia}\right)^2 \sigma^2_{NU} \right] \delta_{ij} \delta_{ab} \tag{3.10}$$

Finally, there is amplification

$$M_{ia} = G^E_i(t) P^{(3)}_{ia} \tag{3.11}$$

associated with the electronics of the APDs which is dependent on time and channel. This includes preamplifier gain, shaper gain, gain associated with the shaping times,

and conversion from voltage to ADC counts. We assume that no signal-dependent noise is introduced during this stage, but there is constant electronic noise $N_i[\tau]$ which has been described above. Additionally, the APDs can contribute noise in the form of a dark current which is uncorrelated with signals; this is inseparable from the electronic noise, and so we absorb it into our description of $N_i[\tau]$.

3.2.2 APD Signals and Noise

We have already characterized the overall gain of the APDs using the lightmap described earlier. We know that a typical single-site deposit of 2615 keV at position $\vec{x}$ and time t will produce a signal with expected magnitude $L_i(\vec{x}, t)$ on APD channel i. We must now connect this empirical understanding of our APD signals with the physical understanding in terms of photons and electrons described above.

We have identified the number of photons created by an event a as $P_a^{(0)}$. In reality, an ideal scintillation measurement can only measure this quantity, and not the true energy of the event – there is randomness in the number of photons produced by a known-energy deposit, so $P_a^{(0)}$ will not be perfectly correlated with the energy E_a of the event. However, the number of photons generated is a difficult parameter to understand empirically, and all of our calibrations occur at a known energy even though the corresponding number of deposited photons is unknown.

Simulations using NEST [11] which have been performed within the EXO group by Liangjian Wen at our bulk electric field indicate that we can expect roughly $82,000$ photons from a 2615-keV gamma deposit. We will identify this parameter

with c, and express the average relation between energy and photon yield in EXO-200 by

$$P^{(0)} = c \cdot E, \tag{3.12}$$

where E is the energy measured in units of 2615 keV. We will treat this relationship as exact, and attempt to measure E rather than $P^{(0)}$; this means that when we speak of measuring the energy of an event using the APD signals, we really are referring to measuring the "scintillation energy," or a parameter proportional to the number of emitted photons which on average will equal the true energy of the deposit.

Ignoring variances for a moment, we can combine equations 3.5, 3.7, 3.9, 3.11, and 3.12 to state that on average,

$$M_{ia} = 1.9 \cdot c f_i(\vec{x}_a) G_i^P(t_a) G_i^E(t_a) E_a.$$

We can compare this to our empirical lightmap measurements, which are expressed by $M_{ia} = L_i(\vec{x}_a, t_a) E_a$, and we conclude that:

$$L_i(\vec{x}, t) = 1.9 \cdot c f_i(\vec{x}) G_i^P(t) G_i^E(t). \tag{3.13}$$

We recall that it is assumed the lightmap is a separable function, $L_i(\vec{x}, t) = R_i(\vec{x}) S_i(t)$, and we can provide the two proportionalities:

$$R_i(\vec{x}) \propto f_i(\vec{x})$$

$$S_i(t) \propto G_i^P(t) G_i^E(t).$$

Although $G_i^E(t)$ is in principle time-dependent, due to environmental effects on the APD electronics and occasional replacement of electronics cards for certain

channels, precision data on its value is not readily available. Instead, we use a time-independent estimate

$$G_i^E(t) = 1.1 \cdot 10^{-3} \tag{3.14}$$

ADC counts per electron emitted from the APD; the uncertainty in this figure is dominated by uncertainty in the preamplifier gains, which are controlled by a roughly 5 pF capacitor. Other contributors to the gain include shaper gain of 21.2 (from a combination of amplification and shaping) and a full-scale digitizer range of 2.5 volts for 12-bit digitization.

We do have independent measurements of the APD gains $G_i^P(t)$ available from laser calibration runs. These special runs allow a laser to shine into the detector from a fixed point and with a stable amplitude while the bias voltages on the APDs are varied from an effective unity gain to our standard voltage settings. Using these measurements, we are able to measure $G_i^P(t)$ at weekly intervals from September 2012 to the present time. Before September 2012, some less-reliable laser data is available, but results from that data are not readily available as of this writing.

It would be possible, and should be a goal for future improvements, to make use of this full range of laser data. However, the laser data provides a less uniform history of APD gains over the full data-taking window of EXO-200 from September 2011 to November 2013, and it is much easier to track time-dependent behavior from Thorium source data which have been collected regularly throughout that period. As a result, a compromise is used to characterize $G_i^P(t)$. One particular laser run, run 4540 (taken on December 13, 2012), is used to fix $G_i^P(t_{4540})$, and the function

is extrapolated using Thorium source data with:

$$G_i^P(t) \approx G_i^P(t_{4540}) \cdot S_i(t)/S_i(t_{4540}).$$

This assumption makes use of the approximation that $G_i^E(t)$ is roughly constant in time, which is probably only accurate to one significant figure; therefore when an electronics change is made to a channel, we can expect that the accuracy of $G_i^P(t)$ is no better than one significant figure. These results mean that we can also estimate with the same level of accuracy:

$$f_i(\vec{x}) \approx \frac{S_i(t_{4540})}{G_i^P(t_{4540})} \cdot \frac{R_i(\vec{x})}{1.9 \cdot cG_i^E(t)}.$$

It is then possible to express the full correlations in signal magnitudes in terms of the scintillation energies of deposits as:

$$\langle M_{ia} \rangle \quad = L_i(\vec{x}_a, t_a)E_a \tag{3.15}$$

$$\langle M_{ia}M_{jb} \rangle = L_i(\vec{x}_a, t_a)L_j(\vec{x}_b, t_b)E_aE_b \left[1 + \frac{\sigma_{NU}^2}{(G_i^P(t))^2}\delta_{ij}\delta_{ab}\right]$$

$$- L_i(\vec{x}_a, t_a)L_j(\vec{x}_a, t_a)E_a\delta_{ab}/c$$

$$+ L_i(\vec{x}_a, t_a)G_i^E(t)E_a\delta_{ij}\delta_{ab}\left[(0.1 + 1.9)\,G_i^P(t) + \frac{\sigma_{G_i}^2(t)}{G_i^P(t)}\right]. \tag{3.16}$$

We combine this with our knowledge of the noise coefficients:

$$\left\langle \widetilde{N}_i[f] \right\rangle = 0$$

$$\left\langle \widetilde{N}_i[f]\widetilde{N}_j[g] \right\rangle = \begin{cases} 0 \text{ if } f \neq g \\ \\ \text{known if } f = g \end{cases}$$

and can claim to now have a complete description of the signals and noise observed in the APD channels.

3.3 Derivation

It is now possible to specify the optimization criteria for generating an energy estimate from the APD signals. We wish to identify an energy estimator which is unbiased and has a minimal expected error. For the problem to remain tractable, we will demand that the operator be linear. Furthermore, although the Fourier-transformed waveforms $\widetilde{X}_i[f]$ are complex-valued, we will require that the energy estimate be strictly real-valued.

We will therefore take the energy estimator to be of the form:

$$\widehat{E}_a = \sum_{if} A_{ifa}\widetilde{X}_i^R[f] + B_{ifa}\widetilde{X}_i^I[f]. \tag{3.17}$$

The goal of denoising is therefore reduced to identifying the optimal parameters A_{ifa} and B_{ifa} for this estimator.

The error in the energy estimate $\widehat{E}_a$ of E_a is defined by:

$$\epsilon_a^2 = \left\langle \left(\widehat{E}_a - E_a\right)^2 \right\rangle. \tag{3.18}$$

Our goal is then to minimize ϵ_a^2 under the constraint of no bias, ie. that:

$$\left\langle \widehat{E}_a - E_a \right\rangle = 0 \tag{3.19}$$

or, equivalently,

$$\sum_{ifb} \left[A_{ifa}\widetilde{Y}_{ib}^R[f] + B_{ifa}\widetilde{Y}_{ib}^I[f] \right] L_i(\vec{x}_b, t_b)E_b = E_a.$$

However, we will find that it is necessary to specify a slightly stronger constraint. In particular, it will be desirable to ensure that the constraints are as independent of

energy as possible to reduce the need to input an estimated energy into our energy estimator; therefore we will freely employ the stronger constraint

$$\sum_{if} \left[A_{ifa} \widetilde{Y}_{ib}^R[f] + B_{ifa} \widetilde{Y}_{ib}^I[f] \right] L_i(\vec{x}_b, t_b) = \delta_{ab} \text{ for all b,} \tag{3.20}$$

which implies the earlier forms and leads to advantageous cancellations of terms.

We now proceed with the optimization. We start by expanding ϵ_a^2:

$$\epsilon_a^2 = \left\langle \left(\widehat{E}_a - E_a \right)^2 \right\rangle$$

$$= \left\langle \widehat{E}_a^2 \right\rangle - E_a \left\langle \widehat{E}_a \right\rangle - \left\langle \widehat{E}_a - E_a \right\rangle E_a$$

We can employ the constraint of equation 3.19 to simplify the second term of this expansion, and eliminate the third altogether; we then proceed:

$$\epsilon_a^2 = \left\langle \widehat{E}_a^2 \right\rangle - E_a^2$$

$$= \left\langle \left(\sum_{if} \left[A_{ifa} \widetilde{X}_i^R[f] + B_{ifa} \widetilde{X}_i^I[f] \right] \right)^2 \right\rangle - E_a^2$$

$$= \left\langle \left(\sum_{if} \left[A_{ifa} \widetilde{N}_i^R[f] + B_{ifa} \widetilde{N}_i^I[f] \right] \right. \right.$$

$$\left. \left. + \sum_{ifb} \left[A_{ifa} \widetilde{Y}_{ib}^R[f] + B_{ifa} \widetilde{Y}_{ib}^I[f] \right] M_{ib} \right)^2 \right\rangle - E_a^2$$

The noise $\widetilde{N}$ and signal M_{ia} are uncorrelated, so multiplicative cross-terms will have an expectation value of zero:

$$\epsilon_a^2 = \left\langle \left(\sum_{if} \left[A_{ifa} \widetilde{N}_i^R[f] + B_{ifa} \widetilde{N}_i^I[f] \right] \right)^2 \right\rangle$$

$$+ \left\langle \left(\sum_{ifb} \left[A_{ifa} \widetilde{Y}_{ib}^R[f] + B_{ifa} \widetilde{Y}_{ib}^I[f] \right] M_{ib} \right)^2 \right\rangle - E_a^2$$

Additionally, electronic noise cross-terms between different frequencies will not survive:

$$
\begin{aligned}
\epsilon_a^2 &= \left\langle \sum_{ijf} \left[A_{ifa}\widetilde{N}_i^R[f] + B_{ifa}\widetilde{N}_i^I[f] \right] \left[A_{jfa}\widetilde{N}_j^R[f] + B_{jfa}\widetilde{N}_j^I[f] \right] \right\rangle \\
&\quad + \left\langle \left(\sum_{ifb} \left[A_{ifa}\widetilde{Y}_{ib}^R[f] + B_{ifa}\widetilde{Y}_{ib}^I[f] \right] M_{ib} \right)^2 \right\rangle - E_a^2 \\
&= \sum_{ijf} \left[A_{ifa}A_{jfa} \left\langle \widetilde{N}_i^R[f]\widetilde{N}_j^R[f] \right\rangle + A_{ifa}B_{jfa} \left\langle \widetilde{N}_i^R[f]\widetilde{N}_j^I[f] \right\rangle \right. \\
&\qquad\qquad \left. + B_{ifa}A_{jfa} \left\langle \widetilde{N}_i^I[f]\widetilde{N}_j^R[f] \right\rangle + B_{ifa}B_{jfa} \left\langle \widetilde{N}_i^I[f]\widetilde{N}_j^I[f] \right\rangle \right] \\
&\quad + \sum_{\substack{ifb \\ jgc}} \left[A_{ifa}\widetilde{Y}_{ib}^R[f] + B_{ifa}\widetilde{Y}_{ib}^I[f] \right] \left[A_{jga}\widetilde{Y}_{jc}^R[g] + B_{jga}\widetilde{Y}_{jc}^I[g] \right] \langle M_{ib}M_{jc} \rangle - E_a^2
\end{aligned}
$$

We will now expand $\langle M_{ib}M_{jc}\rangle$ using equation 3.16 and take advantage of the stronger

form of our constraint 3.20 to simplify the expression:

$$
\epsilon_a^2 = \sum_{ijf}\left[A_{ifa}A_{jfa}\left\langle\widetilde{N}_i^R[f]\widetilde{N}_j^R[f]\right\rangle + A_{ifa}B_{jfa}\left\langle\widetilde{N}_i^R[f]\widetilde{N}_j^I[f]\right\rangle\right.
$$

$$
\left. + B_{ifa}A_{jfa}\left\langle\widetilde{N}_i^I[f]\widetilde{N}_j^R[f]\right\rangle + B_{ifa}B_{jfa}\left\langle\widetilde{N}_i^I[f]\widetilde{N}_j^I[f]\right\rangle\right]
$$

$$
+ \left(\sum_{ifb}\left[A_{ifa}\widetilde{Y}_{ib}^R[f] + B_{ifa}\widetilde{Y}_{ib}^I[f]\right]L_i(\vec{x}_b,t_b)E_b\right)^2 - E_a^2
$$

$$
- \sum_{b}\left(\sum_{if}\left[A_{ifa}\widetilde{Y}_{ib}^R[f] + B_{ifa}\widetilde{Y}_{ib}^I[f]\right]L_i(\vec{x}_b,t_b)\right)^2\frac{E_b}{c}
$$

$$
+ \sum_{ifgb}\left[A_{ifa}\widetilde{Y}_{ib}^R[f] + B_{ifa}\widetilde{Y}_{ib}^I[f]\right]\left[A_{iga}\widetilde{Y}_{ib}^R[g] + B_{iga}\widetilde{Y}_{ib}^I[g]\right]\cdot
$$

$$
L_i(\vec{x}_b,t_b)E_b\left[(0.1+1.9)G_i^E(t_b)G_i^P(t_b)\right.
$$

$$
\left. + \frac{G_i^E(t_b)}{G_i^P(t_b)}\sigma_{G_i}^2(t_b) + L_i(\vec{x}_b,t_b)E_b\frac{\sigma_{NU}^2}{(G_i^P(t_b))^2}\right]
$$

$$
= \sum_{ijf}\left[A_{ifa}A_{jfa}\left\langle\widetilde{N}_i^R[f]\widetilde{N}_j^R[f]\right\rangle + A_{ifa}B_{jfa}\left\langle\widetilde{N}_i^R[f]\widetilde{N}_j^I[f]\right\rangle\right.
$$

$$
\left. + B_{ifa}A_{jfa}\left\langle\widetilde{N}_i^I[f]\widetilde{N}_j^R[f]\right\rangle + B_{ifa}B_{jfa}\left\langle\widetilde{N}_i^I[f]\widetilde{N}_j^I[f]\right\rangle\right]
$$

$$
+ \sum_{ib}\left(\sum_{f}\left[A_{ifa}\widetilde{Y}_{ib}^R[f] + B_{ifa}\widetilde{Y}_{ib}^I[f]\right]\right)^2\cdot
$$

$$
L_i(\vec{x}_b,t_b)E_b\left[(0.1+1.9)G_i^E(t_b)G_i^P(t_b)\right.
$$

$$
\left. + \frac{G_i^E(t_b)}{G_i^P(t_b)}\sigma_{G_i}^2(t_b) + L_i(\vec{x}_b,t_b)E_b\frac{\sigma_{NU}^2}{(G_i^P(t_b))^2}\right]
$$

$$
- \frac{E_a}{c}
$$

We are now in a position to evaluate the partial derivatives of ϵ_a^2 with respect

to the parameters A_{ifa} and B_{ifa}. They are:

$$\frac{\partial \epsilon_a^2}{\partial A_{ifa}} = 2 \sum_j \left[A_{jfa} \left\langle \widetilde{N}_i^R[f] \widetilde{N}_j^R[f] \right\rangle + B_{jfa} \left\langle \widetilde{N}_i^R[f] \widetilde{N}_j^I[f] \right\rangle \right]$$

$$+ 2 \sum_{gb} E_b \widetilde{Y}_{ib}^R[f] L_i(\vec{x}_b, t_b) \left[A_{iga} \widetilde{Y}_{ib}^R[g] + B_{iga} \widetilde{Y}_{ib}^I[g] \right] \cdot$$

$$\left[(0.1 + 1.9) G_i^E(t_b) G_i^P(t_b) \right.$$

$$\left. + \frac{G_i^E(t_b)}{G_i^P(t_b)} \sigma_{G_i}^2(t_b) + L_i(\vec{x}_b, t_b) E_b \frac{\sigma_{NU}^2}{(G_i^P(t_b))^2} \right]$$

$$\frac{\partial \epsilon_a^2}{\partial B_{ifa}} = 2 \sum_j \left[A_{jfa} \left\langle \widetilde{N}_i^I[f] \widetilde{N}_j^R[f] \right\rangle + B_{jfa} \left\langle \widetilde{N}_i^I[f] \widetilde{N}_j^I[f] \right\rangle \right]$$

$$+ 2 \sum_{gb} E_b \widetilde{Y}_{ib}^I[f] L_i(\vec{x}_b, t_b) \left[A_{iga} \widetilde{Y}_{ib}^R[g] + B_{iga} \widetilde{Y}_{ib}^I[g] \right] \cdot$$

$$\left[(0.1 + 1.9) G_i^E(t_b) G_i^P(t_b) \right.$$

$$\left. + \frac{G_i^E(t_b)}{G_i^P(t_b)} \sigma_{G_i}^2(t_b) + L_i(\vec{x}_b, t_b) E_b \frac{\sigma_{NU}^2}{(G_i^P(t_b))^2} \right]$$

We will use Lagrange's method to minimize ϵ_a^2 while satisfying our constraints; we define

$$C_{ab} = \sum_{if} \left[A_{ifa} \widetilde{Y}_{ib}^R[f] + B_{ifa} \widetilde{Y}_{ib}^I[f] \right] L_i(\vec{x}_b, t_b),$$

with ordered indices, and restate the constraints of equation 3.20 as

$$C_{ab} = \delta_{ab}.$$

Then, the partial derivatives of these constrained expressions are:

$$\frac{\partial C_{bc}}{\partial A_{ifa}} = \widetilde{Y}_{ic}^R[f] L_i(\vec{x}_c, t_c) \delta_{ab}$$

$$\frac{\partial C_{bc}}{\partial B_{ifa}} = \widetilde{Y}_{ic}^I[f] L_i(\vec{x}_c, t_c) \delta_{ab}$$

Denoting the set of Lagrange multipliers for ϵ_a^2 with λ_{ab}, where the indices are ordered, and allowing these parameters to absorb constant factors, we can at last

31

identify the full set of linear equations describing the optimal energy estimator $\widehat{E}_a$:

$$\sum_j \left[A_{jfa} \left\langle \widetilde{N}_i^R[f]\widetilde{N}_j^R[f] \right\rangle + B_{jfa} \left\langle \widetilde{N}_i^R[f]\widetilde{N}_j^I[f] \right\rangle \right]$$

$$+ \sum_{gb} E_b \widetilde{Y}_{ib}^R[f] L_i(\vec{x}_b, t_b) \left[A_{iga}\widetilde{Y}_{ib}^R[g] + B_{iga}\widetilde{Y}_{ib}^I[g] \right] \cdot$$

$$\left[(0.1 + 1.9)G_i^E(t_b)G_i^P(t_b) + \frac{G_i^E(t_b)}{G_i^P(t_b)}\sigma_{G_i}^2(t_b) + L_i(\vec{x}_b, t_b)E_b\frac{\sigma_{NU}^2}{(G_i^P(t_b))^2} \right]$$

$$+ \sum_b \lambda_{ab}\widetilde{Y}_{ib}^R[f] L_i(\vec{x}_b, t_b) = 0 \qquad\qquad \text{for each } i, \, f$$

$$\sum_j \left[A_{jfa} \left\langle \widetilde{N}_i^I[f]\widetilde{N}_j^R[f] \right\rangle + B_{jfa} \left\langle \widetilde{N}_i^I[f]\widetilde{N}_j^I[f] \right\rangle \right]$$

$$+ \sum_{gb} E_b \widetilde{Y}_{ib}^I[f] L_i(\vec{x}_b, t_b) \left[A_{iga}\widetilde{Y}_{ib}^R[g] + B_{iga}\widetilde{Y}_{ib}^I[g] \right] \cdot$$

$$\left[(0.1 + 1.9)G_i^E(t_b)G_i^P(t_b) + \frac{G_i^E(t_b)}{G_i^P(t_b)}\sigma_{G_i}^2(t_b) + L_i(\vec{x}_b, t_b)E_b\frac{\sigma_{NU}^2}{(G_i^P(t_b))^2} \right]$$

$$+ \sum_b \lambda_{ab}\widetilde{Y}_{ib}^I[f] L_i(\vec{x}_b, t_b) = 0 \qquad\qquad \text{for each } i, \, f$$

$$\sum_{if} \left[A_{ifa}\widetilde{Y}_{ib}^R[f] + B_{ifa}\widetilde{Y}_{ib}^I[f] \right] L_i(\vec{x}_b, t_b) = \delta_{ab} \qquad \text{for each } b$$

To simplify the notation, let us define a new function:

$$q(i, b) := \left((0.1 + 1.9)G_i^E(t_b)G_i^P(t_b) + \frac{G_i^E(t_b)}{G_i^P(t_b)}\sigma_{G_i}^2(t_b) \right. \qquad (3.21)$$

$$\left. + L_i(\vec{x}_b, t_b)E_b\frac{\sigma_{NU}^2}{(G_i^P(t_b))^2} \right) L_i(\vec{x}_b, t_b)E_b$$

which we note should be strictly positive if measured correctly (because all gains

and lightmap values should be strictly positive, and all variances are non-negative).

Using this shorthand, we can re-write our system of equations in the more compact

form:

$$\sum_j \left[A_{jfa} \left\langle \widetilde{N}_i^R[f] \widetilde{N}_j^R[f] \right\rangle + B_{jfa} \left\langle \widetilde{N}_i^R[f] \widetilde{N}_j^I[f] \right\rangle \right]$$

$$+ \sum_{gb} \widetilde{Y}_{ib}^R[f] q(i,b) \left[A_{iga} \widetilde{Y}_{ib}^R[g] + B_{iga} \widetilde{Y}_{ib}^I[g] \right]$$

$$+ \sum_b \lambda_{ab} \widetilde{Y}_{ib}^R[f] L_i(\vec{x}_b, t_b) = 0 \qquad \text{for each } i,\, f \qquad (3.22a)$$

$$\sum_j \left[A_{jfa} \left\langle \widetilde{N}_i^I[f] \widetilde{N}_j^R[f] \right\rangle + B_{jfa} \left\langle \widetilde{N}_i^I[f] \widetilde{N}_j^I[f] \right\rangle \right]$$

$$+ \sum_{gb} \widetilde{Y}_{ib}^I[f] q(i,b) \left[A_{iga} \widetilde{Y}_{ib}^R[g] + B_{iga} \widetilde{Y}_{ib}^I[g] \right]$$

$$+ \sum_b \lambda_{ab} \widetilde{Y}_{ib}^I[f] L_i(\vec{x}_b, t_b) = 0 \qquad \text{for each } i,\, f \qquad (3.22b)$$

$$\sum_{if} \left[A_{ifa} \widetilde{Y}_{ib}^R[f] + B_{ifa} \widetilde{Y}_{ib}^I[f] \right] L_i(\vec{x}_b, t_b) = \delta_{ab} \qquad \text{for each } b \qquad (3.22c)$$

It is important to note here that energies E_b, which we are intending to measure, do in fact enter into this linear set of equations. At first this would seem to demonstrate that the equations here are impossible to apply, but in fact they remind us that the forms of noise which are correlated with the signal are also dependent on the magnitude of that signal. Statistical fluctuations in the number of photons observed on each APD, for instance, scale like the square root of the number of photons emitted.

We can see, then, that some estimate of energy is necessary to know the relative importance of different forms of noise. But the constraint equation does ensure that our estimate will be unbiased regardless of what energy estimates are fed into the system of equations, so we can be confident that it is only a rough estimate of the energy scale which is needed, and not worry that the optimization will be biased to

estimate energies similar to the estimates we feed in. For this purpose, it is sufficient to use the charge-only energy as an estimate of the scintillation-only energy.

3.4 Matrix Version

Because the system of equations above is linear in A_{ifa} and B_{ifa}, we wish to solve it as a matrix equation. This requires, first, that we choose an ordering of the unknowns; the best ordering will be the one which groups nonzero entries into blocks, since this will allow us to make more efficient use of matrix libraries. We define:

$$\vec{A}_a = (A_{11a}, B_{11a}, A_{21a}, B_{21a}, \ldots, B_{i_{max}1a}, A_{12a}, \ldots, A_{1f_{max}a}, A_{2f_{max}a}, \ldots, A_{i_{max}f_{max}a})$$

$$(3.23)$$

so that the entries alternate between A and B, iterating quickly through channels and more slowly through frequencies. Note that only the A terms are included for the maximum frequency; this is because $X_i[t]$ is real-valued, so $\widetilde{X}_i[0]$ and $\widetilde{X}_i[f_{max}]$ are real-valued as well. We also will find it convenient to define the matrix:

$$\mathbf{A} = \begin{pmatrix} \vdots & & \vdots \\ \vec{A}_1 & \cdots & \vec{A}_{a_{max}} \\ \vdots & & \vdots \end{pmatrix} \tag{3.24}$$

which includes the parameters needed for each of the estimators $\widehat{E}_a$.

We can then define the electronic noise blocks as:

$$\mathbf{N_f} = \begin{cases} \mathbf{COV}\left(\widetilde{N}_1^R[f], \widetilde{N}_1^I[f], \widetilde{N}_2^R[f], \ldots, \widetilde{N}_{i_{max}}^I[f]\right) & \text{for } f < f_{max} \\ \mathbf{COV}\left(\widetilde{N}_1^R[f], \widetilde{N}_2^R[f], \ldots, \widetilde{N}_{i_{max}}^R[f]\right) & \text{for } f = f_{max} \end{cases} \tag{3.25}$$

where **COV** specifies the covariance matrix of an ordered list of random variables,

$$\mathbf{COV}\,(x_1, x_2, \ldots, x_n) = \begin{pmatrix} cov(x_1 x_1) & cov(x_1 x_2) & \cdots & cov(x_1 x_n) \\ cov(x_2 x_1) & cov(x_2 x_2) & \cdots & cov(x_2 x_n) \\ \vdots & \vdots & \ddots & \vdots \\ cov(x_n x_1) & cov(x_n x_2) & \cdots & cov(x_n x_n) \end{pmatrix}. \tag{3.26}$$

Note that because our noise variables $\widetilde{N}_i^R[f]$ and $\widetilde{N}_i^I[f]$ have mean zero, we can move smoothly between expectation values of products and covariances:

$$\begin{aligned} cov(\widetilde{N}_i^R[f], \widetilde{N}_j^R[f]) &= \left\langle \widetilde{N}_i^R[f]\widetilde{N}_j^R[f] \right\rangle \\ cov(\widetilde{N}_i^R[f], \widetilde{N}_j^I[f]) &= \left\langle \widetilde{N}_i^R[f]\widetilde{N}_j^I[f] \right\rangle \\ cov(\widetilde{N}_i^I[f], \widetilde{N}_j^R[f]) &= \left\langle \widetilde{N}_i^I[f]\widetilde{N}_j^R[f] \right\rangle \\ cov(\widetilde{N}_i^I[f], \widetilde{N}_j^I[f]) &= \left\langle \widetilde{N}_i^I[f]\widetilde{N}_j^I[f] \right\rangle. \end{aligned} \tag{3.27}$$

We pack together the blocks of equation 3.25 into a sparse noise matrix:

$$\mathbf{N} = \begin{pmatrix} \mathbf{N_1} & \mathbf{0} & \ldots & \mathbf{0} \\ \mathbf{0} & \mathbf{N_2} & \ldots & \mathbf{0} \\ \vdots & \vdots & \ddots & \vdots \\ \mathbf{0} & \mathbf{0} & \ldots & \mathbf{N_{f_{max}}} \end{pmatrix}. \tag{3.28}$$

In a similar way, we can define the other noise terms in terms of matrix operations. We will find that it is possible to describe the noise terms correlated with signals as a product of two matrices, $\mathbf{P} = \mathbf{P_1}\mathbf{P_2}$. First we define the matrix $\mathbf{P_1}$, which steps horizontally through the APD channels and signals. For a particular

choice of indices j, b, the corresponding column of $\mathbf{P_1}$ will be:

$$\mathbf{P_1}(\text{column } j, \, b) = \begin{pmatrix} \widetilde{Y}_{jb}^{R}[1]\delta_{1j} \\ \widetilde{Y}_{jb}^{I}[1]\delta_{1j} \\ \widetilde{Y}_{jb}^{R}[1]\delta_{2j} \\ \vdots \\ \widetilde{Y}_{jb}^{I}[1]\delta_{i_{max}j} \\ \widetilde{Y}_{jb}^{R}[2]\delta_{1j} \\ \vdots \\ \widetilde{Y}_{jb}^{R}[f_{max}]\delta_{1j} \\ \widetilde{Y}_{jb}^{R}[f_{max}]\delta_{2j} \\ \vdots \\ \widetilde{Y}_{jb}^{R}[f_{max}]\delta_{i_{max}j} \end{pmatrix} \sqrt{q(j,b)}. \tag{3.29}$$

Note that in each column, only a small subset of the entries are nonzero.

This means that $\mathbf{P_2}$ should be a matrix with rows that step through the APD channels and signals as well. For a particular choice of indices j, b, the corresponding row of $\mathbf{P_2}$ will be:

$$\mathbf{P_2}(\text{row } j, \, b) =$$

$$\begin{pmatrix} \widetilde{Y}_{jb}^{R}[1]\delta_{1j} & \widetilde{Y}_{jb}^{I}[1]\delta_{1j} & \widetilde{Y}_{jb}^{R}[1]\delta_{2j} & \cdots & \widetilde{Y}_{jb}^{I}[1]\delta_{i_{max}j} & \widetilde{Y}_{jb}^{R}[2]\delta_{1j} & \cdots \\ \cdots & \widetilde{Y}_{jb}^{R}[f_{max}]\delta_{1j} & \widetilde{Y}_{jb}^{R}[f_{max}]\delta_{2j} & \cdots & \widetilde{Y}_{jb}^{R}[f_{max}]\delta_{i_{max}j} \end{pmatrix} \sqrt{q(j,b)}. \tag{3.30}$$

Since we will be using the product $\mathbf{P} = \mathbf{P_1}\mathbf{P_2}$, it clearly must be the case that the ordering of columns in $\mathbf{P_1}$ is the same as the ordering of rows in $\mathbf{P_2}$. Because in practice there will always be more APD channels than APD signals, it will generally

36

be advantageous to iterate through j fastest, and step through b more slowly. We can also see that $\mathbf{P_1} = \mathbf{P_2}^\top$, so

$$\mathbf{P} = \mathbf{P_2}^\top \mathbf{P_2}. \tag{3.31}$$

The constraint equations are represented by a matrix $\mathbf{C}$ with rows that step through the APD signals; for a particular choice of b the corresponding row of $\mathbf{C}$ will be:

$$\mathbf{C}(\text{row } b) = \left(\begin{array}{ccc} \widetilde{Y}_{1b}^R[1]L_1(\vec{x}_b, t_b) & \widetilde{Y}_{1b}^I[1]L_1(\vec{x}_b, t_b) & \widetilde{Y}_{2b}^R[1]L_2(\vec{x}_b, t_b) \\ \\ \cdots & \widetilde{Y}_{i_{max}b}^I[1]L_{i_{max}}(\vec{x}_b, t_b) & \widetilde{Y}_{1b}^R[2]L_1(\vec{x}_b, t_b) \\ \\ \cdots & \widetilde{Y}_{1b}^R[f_{max}]L_1(\vec{x}_b, t_b) & \widetilde{Y}_{2b}^R[f_{max}]L_2(\vec{x}_b, t_b) \\ \\ & \cdots & \widetilde{Y}_{i_{max}b}^R[f_{max}]L_{i_{max}}(\vec{x}_b, t_b) \end{array} \right).$$
$$\tag{3.32}$$

Finally it is possible to restate the full linear equation specified above in matrix form, where we can simultaneously include the equations for all of the estimators $\widehat{E}_a$:

$$\begin{pmatrix} \mathbf{N} + \mathbf{P} & \mathbf{C}^\top \\ \mathbf{C} & \mathbf{0} \end{pmatrix} \mathbf{A} = \begin{pmatrix} \mathbf{0} \\ \mathbf{I} \end{pmatrix}. \tag{3.33}$$

The matrix $\mathbf{N}$ is the same as the covariance matrix of the electronic noise, so it must be symmetric and positive-semidefinite. Similarly, we have seen that $\mathbf{P} = \mathbf{P_2}^\top \mathbf{P_2}$, implying that $\mathbf{P}$ must be symmetric and positive-semidefinite. This means that there is a Cholesky decomposition $\mathbf{N} + \mathbf{P} = \mathbf{L}\mathbf{L}^\top$, where $\mathbf{L}$ is a lower-triangular matrix, and that $\mathbf{N} + \mathbf{P}$ is symmetric and positive semi-definite. This implies that the full matrix equation is symmetric; however, it is insufficient for

showing that the full system is positive semi-definite, and in fact we will see that this is not the case.

We also note the important observation that this matrix is sparse. Given roughly 1000 frequency components in our signals, only 0.1% of the entries of $\mathbf{N}$ are non-zero. And with 70 APD channels and only a small number of signals we wish to denoise, the combined number of non-zero entries in $\mathbf{P}_1$ and $\mathbf{P}_2$ is easily an order of magnitude less than the number of non-zero entries in $\mathbf{N}$. As a result, we can conclude that this matrix is extremely sparse, and should ensure that whatever method we use to solve these equations takes advantage of this sparsity.

3.5   Preconditioning

We have specified a matrix equation which we now wish to solve. However, it is generally recommended that large matrix equations should not be solved directly. Instead, it is recommended that the matrix should be preconditioned. This means that if a matrix equation $\mathbf{A}\vec{x} = \vec{b}$ should be solved, one should first find a matrix $\mathbf{A}'$ which is approximately equal to $\mathbf{A}$ and which is easily invertible. Finding the right balance between the quality of the approximation $\mathbf{A}' \approx \mathbf{A}$ and the difficulty of computing the inverse $(\mathbf{A}')^{-1}$ is more art than science, but we will present here a preconditioning matrix which seems to strike a good balance for this particular system.

The matrix equation we wish to solve takes the form:

$$
\begin{pmatrix} \mathbf{N} + \mathbf{P} & \mathbf{C}^\top \\ \mathbf{C} & \mathbf{0} \end{pmatrix} \mathbf{A} = \begin{pmatrix} \mathbf{0} \\ \mathbf{I} \end{pmatrix}
$$

Let us define $\mathbf{D} = diag(\mathbf{N})$ and approximate

$$
\begin{pmatrix} \mathbf{N} + \mathbf{P} & \mathbf{C}^\top \\ \mathbf{C} & \mathbf{0} \end{pmatrix} \approx \begin{pmatrix} \mathbf{D} & \mathbf{C}^\top \\ \mathbf{C} & \mathbf{0} \end{pmatrix}
\tag{3.34}
$$

This approximate form is easy to invert (assuming every frequency component of every channel has non-zero noise and every constraint is satisfiable, which is true in practice), and can be used to precondition our problem for better numerical behavior.

We can further factor this approximate form of the matrix:

$$
\begin{aligned}
\begin{pmatrix} \mathbf{D} & \mathbf{C}^\top \\ \mathbf{C} & \mathbf{0} \end{pmatrix} &= \begin{pmatrix} \mathbf{D}^{1/2} & \mathbf{0} \\ \mathbf{C}\mathbf{D}^{-1/2} & \mathbf{H} \end{pmatrix} \begin{pmatrix} \mathbf{D}^{1/2} & \mathbf{D}^{-1/2}\mathbf{C}^\top \\ \mathbf{0} & -\mathbf{H}^\top \end{pmatrix} \\
&= \begin{pmatrix} \mathbf{D}^{1/2} & \mathbf{0} \\ \mathbf{0} & \mathbf{I} \end{pmatrix} \begin{pmatrix} \mathbf{I} & \mathbf{0} \\ \mathbf{C}\mathbf{D}^{-1/2} & \mathbf{H} \end{pmatrix} \begin{pmatrix} \mathbf{I} & \mathbf{D}^{-1/2}\mathbf{C}^\top \\ \mathbf{0} & -\mathbf{H}^\top \end{pmatrix} \begin{pmatrix} \mathbf{D}^{1/2} & \mathbf{0} \\ \mathbf{0} & \mathbf{I} \end{pmatrix}
\end{aligned}
\tag{3.35}
$$

where $\mathbf{H}$ is a lower-diagonal square matrix defined uniquely as the Cholesky decomposition $\mathbf{H}\mathbf{H}^\top = \mathbf{C}\mathbf{D}^{-1}\mathbf{C}^\top$. (The solution is guaranteed to be real because $\mathbf{D}$ is positive-semidefinite in all cases, and positive-definite in practice – it consists of noise variance terms, which are strictly positive in practice.) Note that $\mathbf{C}\mathbf{D}^{-1}\mathbf{C}^\top$ has dimensions equal to the number of signals in an event, which in practice will be small enough that we can compute its Cholesky decomposition $\mathbf{H}\mathbf{H}^\top$ directly.

The two diagonal factors are easily inverted; we further define

$$\mathbf{K}_1 = \begin{pmatrix} \mathbf{I} & \mathbf{0} \\ \mathbf{CD}^{-1/2} & \mathbf{H} \end{pmatrix} \qquad \mathbf{K}_1^{-1} = \begin{pmatrix} \mathbf{I} & \mathbf{0} \\ -\mathbf{H}^{-1}\mathbf{CD}^{-1/2} & \mathbf{H}^{-1} \end{pmatrix} \qquad (3.36)$$

$$\mathbf{K}_2 = \begin{pmatrix} \mathbf{I} & \mathbf{D}^{-1/2}\mathbf{C}^\top \\ \mathbf{0} & -\mathbf{H}^\top \end{pmatrix} \qquad \mathbf{K}_2^{-1} = \begin{pmatrix} \mathbf{I} & \mathbf{D}^{-1/2}\mathbf{C}^\top\mathbf{H}^{-\top} \\ \mathbf{0} & -\mathbf{H}^{-\top} \end{pmatrix}, \qquad (3.37)$$

where $\mathbf{M}^{-\top}$ represents the inverse of the transpose of $\mathbf{M}$. We then follow the standard proscription for preconditioning a linear system by replacing our original matrix equation with the new form:

$$\mathbf{K}_1^{-1} \begin{pmatrix} \mathbf{D}^{-1/2} & \mathbf{0} \\ \mathbf{0} & \mathbf{I} \end{pmatrix} \begin{pmatrix} \mathbf{N}+\mathbf{P} & \mathbf{C}^\top \\ \mathbf{C} & \mathbf{0} \end{pmatrix} \begin{pmatrix} \mathbf{D}^{-1/2} & \mathbf{0} \\ \mathbf{0} & \mathbf{I} \end{pmatrix} \mathbf{K}_2^{-1}\widetilde{\mathbf{A}} = \mathbf{K}_1^{-1} \begin{pmatrix} \mathbf{D}^{-1/2} & \mathbf{0} \\ \mathbf{0} & \mathbf{I} \end{pmatrix} \begin{pmatrix} \mathbf{0} \\ \mathbf{I} \end{pmatrix}$$

$$\widetilde{\mathbf{A}} = \mathbf{K}_2 \begin{pmatrix} \mathbf{D}^{1/2} & \mathbf{0} \\ \mathbf{0} & \mathbf{I} \end{pmatrix} \mathbf{A}$$

which reduces to

$$\mathbf{K}_1^{-1} \left[\begin{pmatrix} \mathbf{D}^{-1/2}\mathbf{N}\mathbf{D}^{-1/2} & \mathbf{0} \\ \mathbf{0} & \mathbf{0} \end{pmatrix} + \begin{pmatrix} \mathbf{D}^{-1/2}\mathbf{P}\mathbf{D}^{-1/2} & \mathbf{D}^{-1/2}\mathbf{C}^\top \\ \mathbf{CD}^{-1/2} & \mathbf{0} \end{pmatrix} \right] \mathbf{K}_2^{-1}\widetilde{\mathbf{A}} = \begin{pmatrix} \mathbf{0} \\ \mathbf{H}^{-1} \end{pmatrix}$$

$$(3.38)$$

$$\mathbf{A} = \begin{pmatrix} \mathbf{D}^{-1/2} & \mathbf{0} \\ \mathbf{0} & \mathbf{I} \end{pmatrix} \mathbf{K}_2^{-1}\widetilde{\mathbf{A}} \qquad (3.39)$$

This preconditioned set of equations is numerically quite stable. It is also possible to provide an excellent initial guess $\widetilde{\mathbf{A}}_0$ by taking the approximate form of the matrix to be exact, yielding

$$\widetilde{\mathbf{A}}_0 = \begin{pmatrix} \mathbf{0} \\ \mathbf{H}^{-1} \end{pmatrix}$$

40

Based on these various advantages, it is this system which we attempt to solve rather than the original form. Below we define matrices $\mathbf{M}$ and $\mathbf{B}$ for convenience, and summarize the system to be solved:

$$\mathbf{M} = \mathbf{K}_1^{-1} \left[\begin{pmatrix} \mathbf{D}^{-1/2}\mathbf{N}\mathbf{D}^{-1/2} & \mathbf{0} \\ \mathbf{0} & \mathbf{0} \end{pmatrix} + \begin{pmatrix} \mathbf{D}^{-1/2}\mathbf{P}\mathbf{D}^{-1/2} & \mathbf{D}^{-1/2}\mathbf{C}^\top \\ \mathbf{C}\mathbf{D}^{-1/2} & \mathbf{0} \end{pmatrix} \right] \mathbf{K}_2^{-1} \quad (3.40)$$

$$\mathbf{B} = \widetilde{\mathbf{A}}_0 = \begin{pmatrix} \mathbf{0} \\ \mathbf{H}^{-1} \end{pmatrix} \quad (3.41)$$

$$\mathbf{M}\widetilde{\mathbf{A}} = \mathbf{B} \quad (3.42)$$

$$\mathbf{A} = \begin{pmatrix} \mathbf{D}^{-1/2} & \mathbf{0} \\ \mathbf{0} & \mathbf{I} \end{pmatrix} \mathbf{K}_2^{-1}\widetilde{\mathbf{A}} \quad (3.43)$$

3.6 Solver

The matrix $\widetilde{\mathbf{A}}$ for which we attempt to solve will have as many columns as there are signals we wish to denoise within an event; often, this will only be one, and $\widetilde{\mathbf{A}}$ will simply be a column vector. However, there certainly are many events with multiple scintillation signals; we will also later discuss extended applications of denoising where we may treat events as having additional signals. In these cases the number of columns may be larger. In such cases it would be possible to solve for each column of $\widetilde{\mathbf{A}}$ independently, but more efficient to solve the entire system simultaneously. In this way, information obtained from multiplying the matrix by one column may be exploited to solve the other columns as well, effectively multiplying the benefit from each matrix-multiplication by the number of columns of $\widetilde{\mathbf{A}}$.

Matrix-solving algorithms which handle multiple vectors simultaneously are commonly referred to as block algorithms. We will use the Block-BiCGSTAB algorithm [18], an iterative method based on the popular stabilized biconjugate-gradient (BiCGSTAB) method. BiCGSTAB and Block-BiCGSTAB are notable for being able to deal with arbitrary matrices rather than requiring that the matrix be positive-definite (which our matrix is not). The algorithm is reproduced in the form used by our code as Algorithm 1. This algorithm only requires that we are able to left-multiply vectors and matrices by $\mathbf{M}$ quickly, which makes it possible to exploit the sparsity of $\mathbf{M}$.

Since each column of $\widetilde{\mathbf{A}}$ corresponds to one signal we are refitting, the norm of the corresponding column of $\mathbf{R}$ tells us how well we have identified the optimal magnitude estimator for that signal; thus, to test for termination we should evaluate the norm of each column of $\mathbf{R}$, and while any of those norms are above some threshold, the solver must be permitted to continue. Because our resolution is only on the order of 1%, solutions generally need not be very accurate; in practice, we establish reasonable thresholds by plotting resolution against threshold for a small subset of data, and observing when the resolution stops improving.

3.7 Implementation

Although the previous section described the algorithm used for solving these matrix equations, in practice the processing time required is still significant; combined with the very large number of events which we hope to denoise (hundreds of millions), we

Algorithm 1 Block-BiCGSTAB Algorithm
_____

1: $\widetilde{\mathbf{A}} \leftarrow \widetilde{\mathbf{A}}_0$

2: $\mathbf{R} \leftarrow \mathbf{B} - \mathbf{M}\widetilde{\mathbf{A}}$

3: $\mathbf{S} \leftarrow \mathbf{R}$

4: $\widetilde{\mathbf{R}}_0 \leftarrow \mathbf{R}$

5: **loop**

6:      $\mathbf{V} \leftarrow \mathbf{MS}$

7:      Solve $(\widetilde{\mathbf{R}}_0^\top \mathbf{V})\alpha = (\widetilde{\mathbf{R}}_0^\top \mathbf{R})$ for α.

8:      $\mathbf{R} \leftarrow \mathbf{R} - \mathbf{V}\alpha$

9:      $\mathbf{T} \leftarrow \mathbf{MR}$

10:      $\omega \leftarrow \langle \mathbf{T}, \mathbf{S} \rangle_F / \langle \mathbf{T}, \mathbf{T} \rangle_F$, where $\langle \cdot, \cdot \rangle_F$ is the Frobenius matrix norm.

11:      $\widetilde{\mathbf{A}} \leftarrow \widetilde{\mathbf{A}} + \mathbf{S}\alpha + \omega\mathbf{R}$

12:      $\mathbf{R} \leftarrow \mathbf{R} - \omega\mathbf{T}$

13:      $\mathbf{R}$ currently equals $\mathbf{B} - \mathbf{M}\widetilde{\mathbf{A}}$

14:      **if** all columns of $\mathbf{R}$ have sufficiently small magnitudes **then**

15:           **return** $\widetilde{\mathbf{A}}$

16:      **end if**

17:      Solve $(\widetilde{\mathbf{R}}_0^\top \mathbf{V})\beta = -(\widetilde{\mathbf{R}}_0^\top \mathbf{T})$ for β.

18:      $\mathbf{S} \leftarrow \mathbf{R} + (\mathbf{S} - \omega\mathbf{V})\beta$

19: **end loop**
_____

still must seek out any possible speed-ups. There are certain implementation tricks which can be applied with significant impact. These are described here.

The majority of non-zero matrix entries comes from the electronic noise matrix $\mathbf{N}$, making it the computational bottleneck of the algorithm. $\mathbf{N}$ is block-diagonal, as seen in equation 3.28; if we assume roughly 70 APD channels, then the last block of $\mathbf{N}$ will have 70^2 non-zero entries and all other blocks will have $4 \cdot 70^2$ non-zero entries. With waveforms having 2048 samples, and ignoring the baseline component, the problem of multiplying a vector by the electronic noise terms thus consists of 1024 matrix-matrix multiplications, with each left matrix containing roughly $20,000$ non-zero terms and each right matrix consisting of $O(1)$ columns and roughly 150 rows. (The number of columns in the right matrix is equal to the number of signals, which may be sometimes $3 - 5$ or more; however, it is always much smaller than 150, and describing it as $O(1)$ captures this fact.)

The key points here which create an opportunity for optimization are that:

- The electronic noise terms generally do not change event-by-event. They are treated as constant across many runs.

- It is possible to multiply two $N \times N$ matrices together much faster than it is possible to perform N multiplications of an $N \times N$ matrix with N $N \times 1$ matrices. This can be achieved with a combination of algorithms faster than naive $O(N^3)$ speed and exploitation of low-level computer hardware features such as the CPU cache. [3] [17]

What we wish to do, then, is reorganize the solver algorithm so that whenever

multiplication by the electronic noise matrix is required, rather than performing that multiplication on a "skinny" $150 \times O(1)$ matrix, we pack together many such "skinny" matrices into a single matrix with many columns. Multiplication can then be performed in bulk; and individual columns from the result can be extracted and used as before.

Additionally, it is important that matrix multiplication be made as fast as possible. It has long been known that matrix multiplication provides significant opportunities for low-level optimizations. For example, most of the time taken by naive matrix multiplication is spent fetching and writing data to and from RAM. Significant speedups can be achieved by minimizing the number of CPU cache misses, which can be accomplished by operating on matrices in blocks with size chosen so they fit entirely in the cache. Multiplication instructions can also often be packed into vector instructions such as SSE or AVX. For extremely large matrices, there are even algorithms which require fewer than $O(N^3)$ multiplications, and these can sometimes be beneficial. [17]

Optimization of matrix-matrix multiplication is a large field, but fortunately there are a number of well-tuned software libraries implementing matrix multiplication well-tuned to specific machines. These libraries generally provide the standard Basic Linear Algebra Subroutines (BLAS) interface, making them interchangeable with ease. In this instance, Intel's MKL library has been used; benefits to this implementation are its availability on scientific computing platforms and its ability to adapt to heterogeneous compute clusters by detecting the architecture of the machine on which it is run. [21]

Finally, implementation at NERSC has the interesting feature that NERSC's computing systems are designed for multi-core processing. The Hopper and Edison computing systems at NERSC allocate whole nodes, each of which contains 24 cores. Although it is possible to simply run 24 independent processes on each node, memory on NERSC machines is highly constrained; memory use can be reduced by sharing certain large data structures across multiple cores on a node. Additionally, as more events are packed together for electronic-noise multiplication, greater savings can be realized; so it is better to handle many events in coordination. To this purpose, a multi-threaded version of the program has been developed to exploit portions of the code which are conveniently distributed. Because NERSC nodes have a Non-Uniform Memory Access (NUMA) architecture, processes are constrained to only run on cores with a similar memory access pattern; on Hopper this results in four 6-threaded processes per node, while on Edison this results in two 12-threaded processes per node.

As a result, and because the bulk of our computational time is spent multiplying by $\mathbf{N}$, we pursue the following strategies to improve code performance:

1. One denoising process will be run on each NUMA node of a NERSC machine. Processes should be run in "strict memory mode," where a process only has access to memory resources on its own NUMA node.

2. Within a process, algorithm 1 should be performed in parallel on all available cores to maximimize CPU utilization.

3. When a thread encounters the need for a matrix multiplication in lines 2, 6,

or 9, the thread should not multiply by $\mathbf{N}$. Instead, it should push the left hand side into new columns of a matrix $\mathbf{RHS}$ of "thin" matrices needing to be multiplied by $\mathbf{N}$.

4. When enough columns have accumulated in $\mathbf{RHS}$, collect the running threads; these threads should each perform some fraction of the matrix multiplications between blocks of $\mathbf{N}$ and the corresponding rows of $\mathbf{RHS}$. When this is complete, the threads should resume their processing of algorithm 1 in parallel on the available pool of events.

5. Every matrix multiplication should be performed by a direct call to the Intel MKL library. To facilitate this process, $\mathbf{N}$ should be stored in a format that ensures its blocks are accessed in a contiguous segment of memory. Furthermore, because there is ample opportunity for higher-level parallelization, at no time should a multithreaded BLAS operation be invoked; this reduces computational overhead of parallelization.

These represent the most significant set of computational optimizations. However, there are also smaller optimizations which can still produce non-negligible speedups. The naive Block-BiCGSTAB algorithm (in the case of only one signal in an event) requires two matrix-vector multiplications, but it also requires a number of vector-vector operations, and the cumulative cost of these vector-vector operations can become non-negligible. One obvious shortcut is to reuse our computation of $\widetilde{\mathbf{R}}_0^\top \mathbf{V}$ from line 7 of Algorithm 1 to save work in line 17.

Another speedup for our vector-vector operations consists of combining mul-

tiple operations into one step. We see on line 7 that both $\widetilde{\mathbf{R}}_0^\top \mathbf{V}$ and $\widetilde{\mathbf{R}}_0^\top \mathbf{R}$ are computed. As described earlier in the context of multiplication of vectors by electronic noise, it is possible to take advantage of caching and speed up vector operations by packing multiple vectors together into a more square-shaped matrix. In this case, rather than computing these two products separately, we can pack $\mathbf{V}$ and $\mathbf{R}$ together and compute

$$\widetilde{\mathbf{R}}_0^\top \begin{pmatrix} V & R \end{pmatrix}$$

as one step. The rest of the algorithm will not be affected by the fact that these two matrices are stored contiguously in memory.

3.8   Denoising in Practice

The preceding description of denoising has been intended to convey our fullest current understanding of denoising as it should be performed. However, due to the computational intensity of this algorithm it is not feasible to conduct routine data processing of the full EXO-200 dataset whenever updates to the code base are implemented. As a result, the most recent denoised data available from EXO-200 demonstrates certain deviations from the description above. It is known, and has been demonstrated, that correcting some of these flaws can lead to further improvements in resolution, but no physics analysis will be performed with those improvements until the computational cost of denoising is again deemed worthwhile.

In this section we outline the places where the denoising used for the current physics analysis differs from the description above. Differences in implementation

also exist, but will not be described here. The differences of denoising are:

- The signal variance coming from sources internal to the APDs was not fully understood by this author when denoising was first implemented, and as a result the signal variance is significantly underestimated. Specifically, in place of equations 3.8 and 3.10 we take

$$\left\langle P_{ia}^{(3)} P_{jb}^{(3)} \right\rangle = (1.9)^2 \cdot G_i^P(t_a) G_j^P(t_b) \left\langle P_{ia}^{(1)} P_{jb}^{(1)} \right\rangle.$$

- We have described with equation 3.14 that the electronic gain is treated as having a constant value of $1.1 \cdot 10^{-3}$ ADC counts per electron emitted from the APDs. The wires use a similar set of electronics; however, their gain is nominally set to a different value of roughly $6.3 \cdot 10^{-4}$ ADC counts per electron collected on the wires, and this author confused the two numbers. As a result, $G_i^E(t)$ was underestimated by almost a factor of two; the effect of this is to overestimate by almost a factor of two the number of photons being deposited on APDs, which again causes us to underestimate the signal variance introduced within the APDs.

The effect of both of these issues is, loosely speaking, to fool denoising into believing its photon statistics are greater than they truly are; this, in turn, leads it to prefer a higher concentration of signal (more weight on fewer channels) than is ideal. Thus, the resolution is negatively impacted by these mistakes; the impact has been measured in subsets of the the EXO dataset and this negative impact is apparent.

However, neither of these mistakes have any impact on the correctness of the constraints. As a result, the denoised energy measurements should still be unbiased, even if they have worse variance than necessary. Results from the use of this data will be described in chapter 5.

3.9 Future Plans

As outlined here, denoising is capable of producing optimal estimates of the total energy emitted in scintillation by a particular event; however, it should be noted that this algorithm can be applied to a more general range of problems in the EXO-200 detector with only minor modifications.

3.9.1 Anticorrelated Cluster Energies

One important generalization is in our definition of "signals." In the body of this chapter, we have worked on the assumption that a signal consists of a simultaneous set of energy deposits in the bulk of the detector, possibly at multiple locations. We do this because it must be possible for denoising to break degeneracies between signals – by specifying that two different signals must have occurred at different times, we give the algorithm a means to discriminate between light coming from the two different signals and assign energy properly to each of them.

Historically, time was the only useful variable for this sort of discrimination; because multiple APD channels were added together and all APD channels were treated as identical in this sum, a significant amount of information was discarded

and there were no remaining parameters to use for signal separation except for the signal time.

However, this denoising algorithm makes use of additional information: the relative magnitudes of each APD gang. By depending on a highly detailed lightmap, we have incorporated information about which channels should see light most from energy deposits at different positions. As a result, if we permit two "signals" which are simultaneous in time, it should be possible to separate their energy content by comparing their positions to the set of channels which see more light. This would allow us to produce anti-correlated energy measurements of individual clusters, which should give a significant improvement in the energy resolution achievable for clusters within an event.

In principle, this is entirely feasible – in the extreme case, when two clusters are at opposite ends of the detector we can expect them to produce light on an entirely different set of channels, and it should be quite easy to separate light produced by each. However, this extension of our algorithm does present some practical challenges.

In EXO's reconstruction, light signals which are found close together in time are aggressively merged together, ensuring that denoising will never encounter light signals which are very close in time; this assures us that two signals separated in time will be well-separated, and there will not be a near-degeneracy which could render the solver algorithm unstable.

However, charge clusters are merged much less aggressively, and some bugs exist which have minimal effect on the main analysis but permit the existence of

clusters very near to each other. For denoising to separate simultaneous light signals solely based on their relative position, they must be separated far enough that their respective light yields on nearby APD channels are significantly different, which is not at all guaranteed by reconstruction. As a result, denoising can only fit simultanous signals separately if it performs a re-clustering process in which clusters occurring near each other are artificially merged together for the purpose of denoising. The threshold for merging clusters together would require further study, and might be different in each of the three coordinate directions.

Such an analysis would not have a significant impact on single-site data, so it would have minimal impact on our primary goal of searching for double-beta decay. However, it could have a significant impact on a search for excited-state two-neutrino double-beta decay by improving the resolution of gamma lines associated with Barium de-excitation. Barabash states in [2] that the dominant mode of excited-state $2\nu\beta\beta$ decay will be to the 0_1^+ state, which in ^{136}Ba would lead to the emission of a 760 keV and 819 keV gamma in coincidence; if denoising could be accomplished on individual clusters, the sensitivity to these gamma lines could be significantly enhanced.

There are also potential benefits to our understanding of the detector itself. Currently the only mono-energetic beta calibration available for EXO is the double-escape peak, formed when a gamma particle enters the detector, pair-produces an electron and positron, and the positron interacts with an electron and emits gammas which travel sufficiently far from the initial interaction site so that the initial electron interactions and gamma interactions can be clearly separated. Currently we have

the ability to separate charge yield from gammas and the initial electron in some of these events, allowing us to understand the different charge yields from gammas and betas. However, we have no similar capabilities for light yield because the gamma and beta interactions are treated as just one "signal." If we could separate the light yield from these spatially separated clusters, we could use these events to understand both the light and charge yield for different types of interactions.

Another type of detector study which might benefit from anticorrelated cluster energies is the Compton telescope. This is a technique that combines our knowledge of cluster energies and scattering angles, along with the Compton scattering formula [7], which allows us to produce estimates of the origin of the incident gamma. Such a technique permits us to study the sources of our backgrounds, informing future attempts to reduce them by indicating which materials had the most significant negative effect. The accuracy by which we place the origin of the incident gammas is strongly related to the accuracy of our measurements of the energies of the individual clusters, so it is expected that improving the accuracy of our cluster energies would have a positive impact on our ability to locate the backgrounds of our experiment.

The last benefit to this approach is more technical: evaluating the lightmap for a multi-site event requires an energy-weighted combination of the values of the lightmap at individual cluster locations. This process is complicated and error-prone, and can be avoided entirely when we treat each signal instead as having a single well-defined position.

3.9.2 Wire Denoising

The current EXO-200 resolution is limited by the scintillation resolution of the APDs. As a result, little benefit is anticipated from denoising the wires. However, it is possible that a future detector could reduce the scintillation noise to a point where resolution of the wires is non-negligible; alternatively, a future detector could have noise which is correlated between wires and APDs, making it possible to use noise information from the wires to improve our scintillation resolution even though no direct benefit is expected to the wire resolution itself.

In any case, it is possible to apply equations 3.22 to a system with a combination of wires and APDs without significant adjustment. The template functions $Y[t]$ will of course be significantly different, and must include a time offset to account for the different time of arrival of the electrons and photons. The "lightmap" of charge will be far less diffuse than for APDs because charge from any location generally drifts directly to only a small number of wires along externally imposed field lines. And finally, because electron statistics should be negligible and signal amplification should not be a noisy process, for wire channels we would modify equation 3.21 to state that $q(i_{wire}, b) = 0$. In this sense, denoising of wires consists of minimizing the variance in the energy estimator due to electronic noise, and using the wires to improve our denoising of APDs consists of using information about the wires to reduce variance due to electronic noise without expecting any correlations between APD and wire signals, all while ensuring that the energy estimates are unbiased by retaining the same constraints.

Chapter 4:   Noise Measurements

Chapter 5:   The Lightmap

The EXO detector was designed with roughly 450 APDs ganged into 74 data channels of six to seven APDs each. Three of the APD ganged channels were disabled due to noisy components before physics data collection began; a fourth channel was disabled in February 2012 due to increasing noise in its components. All of the APDs were set into the two endcaps of the cylindrical EXO detector. To improve light collection, teflon sheets cover the sides of the detector and reflect light back into the liquid xenon rather than allowing it to be absorbed by the vessel walls.

The different positions of the APDs means that given the same amount of energy deposited into the detector, channels whose APDs are nearest to the deposited energy may show significantly larger signals than channels with APDs far from the deposit. As a result, it is critical to map out the response of the APDs as a function of deposit position $\vec{x}$.

Furthermore, the APDs and APD electronics will show time-dependent changes: gain will drift in each APD at independent rates, and stepwise changes to the APD signals comes from disabling of channels and changes to the electronics which have been implemented multiple times during the course of the experiment. This means

that in addition to mapping the response of the APDs as a function of deposit position $\vec{x}$, we must also map it as a function of deposit time t.

Early attempts to generate this mapping focused on periodic campaigns to collect large amounts of known-energy data and characterize the APD response at a moment in time. These campaigns would generally consist of days of source data. The strong Thorium-228 source would be used, and an expert would be on-site to position the source in a wide range of locations, to ensure that a single campaign was independently sufficient to characterize the APD response. The 2615-keV single-site gamma line of the Thallium-208 daughter product of Thorium-228 was isolated in offline analysis, and signals from these events were used to measure the signal magnitude from a known-energy single-position deposit in the detector.

Even with such a significant quantity of source data, statistics were found to be insufficient. Some regions of the detector were difficult to illuminate, and signals on individual channels were small. To simplify the problem, signals on each endcap were summed together (without gain corrections) so that the 70 or 71 active APD channels could be treated offline as two large-magnitude APD channels instead. This increased the size of the signals; it also made the spatial dependence of the response smoother, so that a sparser distribution of data could still be sufficient to characterize the response. This permitted the creation of an APD-plane lightmap which allowed EXO to produce its first position-dependent corrections to scintillation energy. [20]

Although the APD-plane lightmap produced significant improvements in the energy resolution achieved by the EXO detector, inevitably it was only an incomplete

characterization of the APD response. Indeed, because for $\beta\beta0\nu$ studies we place our fiducial cut as close to the edges of the detector as possible, in certain regions of the detector our scintillation signal might be highly concentrated on one or a small number of channels. Summing together multiple channels is, in this sense, a lossy form of compression of the data, and it is tempting to see whether we can extract better physics if it is avoided. The denoising algorithm described in chapter 3 describes one such analysis which can exploit knowledge of the behavior of individual APD channels; others might include reducing our scintillation thresholds by allowing us to search for signals in subsets of the APDs rather than only in sums across entire endcaps. Thus, characterizing the APD yield on individual APD-gang channels is not in itself an important component of our analysis, but may be expected to provide a critical tool for more advanced scintillation analysis.

5.1   Four-Dimensional Lightmap

As described above, in constructing an individual-APD lightmap we face two conflicting needs: we must use as much data as possible to handle the faster spatial dependence and smaller signals expected, but if too much data is included then we run the risk of combining data taken when an APD or the electronics had a different gain. If we truly wish to use all available data, then we will need to simultaneously understand the full time-dependence of the gain. In other words, rather than forming a small number of independently-measured three-dimensional lightmaps, we will need to measure a four-dimensional lightmap $L(\vec{x}, t)$. Since we will use Thorium-228

source data to generate the lightmap, we require that our lightmap should predict the magnitude of the signals on each APD gang induced by a single-site deposit of energy 2615 keV; figure 3.2 shows our definition of a unit-magnitude signal, which is the same as was used in chapter 3.

This may at first seem infeasible. After all, adding an extra time dimension to the arguments of the lightmap is equivalent to generating a new lightmap for every time bin, which is exactly the situation we wished to avoid. But we can make a key simplifying assumption that the lightmap is separable. In a physical sense, we can assume that:

1. From a given position $\vec{x}$ photons deposit on each APD channel at a constant rate.

2. Each APD channel in turn magnifies and shapes its signal with a gain which may vary in time, but does not depend on the point of origin of the photons.

So, we demand that the lightmap have the much simpler form

$$L(\vec{x}, t) = R(\vec{x})S(t) \tag{5.1}$$

Is this simplification fully motivated by the detector? Although it is a reasonable approximation, there are details which it omits. The first point is fairly accurate: we must trust that the electric field and the reflectivity of detector surfaces are constant in time, but these conditions are assumed to hold within EXO-200.

However, each channel can draw its signal from multiple APDs, each of which has an independent time-varying gain. Photons from a deposit may preferentially

sample the gain from the closest APD within a channel, so deposits in different locations may track more closely the gain of the closest APD within a channel, and the second point may not be accurate. Studying the impact of this effect should be a topic for future study, particularly to understand to what degree it limits the effectiveness of a lightmap; it may be relevant to nEXO planning to understand how ganging together APDs reduces the quality of the approximation of equation 5.1. The current analysis will treat it as a small effect.

So, treating equation 5.1 as valid, one simple general scheme to find R and S iteratively is described in algorithm 2. Step 1 of that algorithm is to select 2615-keV single-site events; it is understood that compton-scattered events will inevitably leak into our selection window, but we use the best available energy measurements to reduce that likelihood and trust that as analysis improvements continue to sharpen our resolution, the number of compton-scattered events leaking through becomes smaller and the quality of the lightmap will continue to improve. The rest of the algorithm then describes how we can efficiently converge on estimates of $R(\vec{x})$ and $S(t)$ through an iterative approach. We do not prove that the algorithm is guaranteed to converge; however, in practice $S(t)$ is close to constant, resulting in fairly rapid convergence.

5.2 Algorithm Details

The previous section outlines a general algorithm for computing a four-dimensional lightmap from source data. In this section we will specify the implementation choices

---
Algorithm 2 Generating a Lightmap

1: Tabulate, using the best energy measurement available, a list of single-site 2615-keV events from Thorium-228 source data.

2: Set $S(t) = 1$ for all APD channels.

3: **repeat**

4:      For each APD channel, estimate $R(\vec{x}) = L(\vec{x}, t)/S(t)$ from the set of events tabulated in line 1.

5:      For each APD channel, estimate $S(t) = L(\vec{x}, t)/R(\vec{x})$ from the set of events tabulated in line 1.

6: **until** convergence is reached.
---

which are made in the code currently being used. In attempt to encourage future experimentation, alternative options will also be listed in some detail, along with some motivations for these alternatives. Time has not permitted testing of all of these options, but it is hoped that they will be explored in the future.

5.2.1   Event Selection

The single-site Thorium-228 spectrum is well-peaked at 2615 keV, making it an excellent monoenergetic calibration line. Our challenge is to select truly 2615-keV events as efficiently as possible, while simultaneously avoiding near-2615-keV events which may leak into the dataset.

This is an inherently iterative process. The first lightmap had to be constructed from an ionization-only spectrum because no useful position-corrected scintillation measurement existed; the resolution of the ionization-only spectrum was

quite poor, roughly 3.5% (sigma) of the energy, as described in Steve Herrin's thesis, and severe compromises had to be made to keep the Compton-shoulder leakage down to acceptable levels. That work required events to have ionization between 0.33σ and 3σ to the right of the ionization peak. [20]

Such a strongly asymmetric cut was chosen to avoid leakage from compton shoulder events, which it did successfully. However, because of anticorrelation between scintillation and ionization, choosing events whose ionization had oscillated high means this cut was also preferring events whose scintillation had oscillated low, introducing a bias in the lightmap magnitude. Additionally, the cut permits less than 37% of desired events to be accepted, which is a substantial loss of efficiency that has a significant impact in certain low-statistics regions of the detector.

The current work has had the benefit of an existing position-corrected scintillation measurement, leading to a rotated energy spectrum with resolution of roughly 1.8%. As a result, it is possible to accept a wider cut (in sigmas) while still keeping Compton shoulder leakage small. We currently accept all events within 2σ of the peak, with better than 95% acceptance and only small leakage. An additional benefit is that this improved resolution allows us to use a symmetric acceptance region, avoiding the implicit bias introduced from the earlier asymmetric cut window.

Preliminary investigations have been conducted to see what impact is observed from using the denoised scintillation measurements which are the subject of this work. Presently the improvement in resolution (to roughly 1.4%) UPDATE WITH REAL NUMBER when the paper is finalized has not demonstrated any significant improvement in the quality of the lightmap beyond what we could achieve with

1.8% resolution; however, this is a topic of continuing study which will certainly be revisited.

Beyond the cuts described above (single-site within an appropriate energy window), other basic cuts are applied to ensure only well-behaved scintillation signals are selected:

- Charge and light must individually lie within a reasonable range.

- The charge-to-light ratio must not identify an event as an alpha decay.

- The scintillation time must be well-separated from any other scintillation signals in same event frame.

- All charge signals which are assigned to this scintillation signal must be assigned unambiguously.

- All three position coordinates must be known. (No fiducial cut is placed, since that would restrict the volume where the lightmap is specified.)

Many of these cuts are probably no longer necessary – as the resolution has improved, the chances of contamination have decreased and we can be a bit less cautious about accepting events. It is worth remembering, though, that our main analysis only accepts events with a single scintillation signal, something which for us would carry too high a cost in lost statistics. (Strong Thorium runs produce a significant rate of events with multiple scintillation signals. These statistics are quite valuable, particularly because they are the primary source of statistics in some hard-to-reach

regions of the detector.) As a result, it is important to maintain some caution with cuts designed to handle those events more robustly.

5.2.2 Function Parametrization

Because we are attempting to empirically measure the functions $R(\vec{x})$ and $S(t)$ from a finite dataset, we need to specify some more limited form for them to take. All current approaches to describing $R(\vec{x})$ first bin the detector volume into three-dimensional voxels, and then define $R(\vec{x})$ to interpolate linearly between known values at the center of the voxels. The size of these voxels must be chosen with some care; if they are too small, then low per-voxel statistics will cause the statistical errors on the signal magnitude to dominate, whereas if the voxels are too large then the spatial variation of the lightmap will not be fully captured.

In the current lightmap, the detector is binned into $1cm^3$ voxels; the detector is easily contained within a box with sides $40cm$ long, leading to $64,000$ voxels (of which roughly 20% lie outside of the detector and will be empty). The choice of voxel size was made based on the size of an individual APD. The APDs are roughly $2.5cm$ in diameter, so very near the anode we would like for the size of a voxel to be much smaller than $2.5cm$. When this is done, much of the detector has entirely sufficient statistics per voxel; however, there are some regions of the detector with fewer than ten hits per voxel, indicating that $R(\vec{x})$ may have quite significant statistical error in these regions.

It is possible to justify a choice of larger voxels. The APDs lie at $\pm 204mm$

from the cathode, which means that there is more than $2cm$ between our fiducial volume and the APDs. At this distance, the dependence of the lightmap on x and y is expected to be much slower than at the APD plane, indicating that perhaps $2cm$ binning in x and y may be sufficient. Additionally, z-dependence of the lightmap is expected to be fairly smooth throughout the detector; since we interpolate linearly between voxels, it may be possible to use a z-binning much coarser than $1cm$. This may be a topic for future investigation.

It is also worth mentioning that less intuitive voxel geometries have been tried in the past. The older APD-plane lightmap [20] used a cylindrical-coordinate binning; binning in r was selected to make the bin volumes roughly constant along the r axis, binning in the angular coordinate was uniform, and binning in z was chosen to be coarser near the anodes and finer near the cathode to reflect faster variation there. In all cases the binning was coarser than with the current cubic voxels being used; our finer binning is made possible by the larger quantity of available statistics from using the full dataset, and is justified by the potential for the yield on a single APD gang to vary more rapidly than the yield averaged across an entire APD plane.

It is well-known [26] that when it is necessary to estimate a multivariate function from limited statistics, a choice of binning can have a significant impact on the result. It is preferable to use an unbinned technique such as kernel regression. In particular, our data density is highly non-uniform, and it should be possible to measure the lightmap which high fidelity in regions of high statistics, while smoothly transitioning to a coarser interpolation in regions of low statistics to minimize the impact of uncertainty from individual hits. State-of-the-art solutions to this problem

would rely on locally adaptive kernel regression; see [26] for a detailed explanation of the related issues in non-parametric multivariate regression. Attempting to use a locally adaptive kernel regression for $R(\vec{x})$ should be considered a highly appealing extension to the algorithm for generating a lightmap.

The parametrization of $S(t)$ presents a very different set of choices. Thorium data is taken in bursts, with the time between mostly filled by low-background runtime. When we choose to treat $S(t)$ as a smoothly varying function, it becomes critical to interpolate properly – after all, the low-background runtime is the critical part of the experiment. (If we only produce a lightmap accurate during source runtime, we will measure an energy resolution from source data which is not borne out in the low-background data, so we should in fact be able to give some guarantee that $S(t)$ is almost as accurate during the low-background runtime as during the source runtime.) Fortunately, it is generally true that the time variation of the APD response is quite slow; exceptions are generally due to changes in the electronics which should occur at well-specified times.

Currently each source run is treated as a burst of data taken at the midpoint of the run, and $S(t)$ is measured at that point only from the data of that run; then $S(t)$ is linearly interpolated between those points. In principle it is possible that between two source runs an electronics change may have been performed, which would mean that a better interpolation would be to assume $S(t)$ is flat except for a step at the time of the electronics change; in practice, though, EXO has generally taken a source run immediately before and after an electronics change, so no high-value data is taken during that interval and this detail can be ignored.

Another concern with this method is what should be done with short source runs. If a run is too short, then the measurement of $S(t)$ coming from that run may have significant errors. We currently mitigate this issue by entirely throwing out all data from runs with fewer than 100 usable events. We justify this approach by claiming that even though those events might in principle have contributed some useful information on $R(\vec{x})$, without a good measurement of the relevant $S(t)$ it is impossible to use that data.

It would be better if we made use of our knowledge that $S(t)$ changes slowly or at well-defined moments. In the future, it would be useful if instead we performed smoothed interpolations between electronics changes. This could be done in the same style as EXO's lifetime corrections, using polynomial fits, where the degree of the polynomial could be determined by eye. A candidate set of time intervals when $S(t)$ might be treated as constant could be the same as the set of constant noise windows described in chapter 4. It would be possible to check whether this time binning is fine enough by looking at the Thorium scintillation peak position versus time in denoised data – if it appears to drift in time within a window where $S(t)$ is treated as constant, then it is likely that $S(t)$ needs to be binned more finely.

Alternatively, often there will be a long string of consecutive source runs which should be combined into one higher-statistics dataset. This process would need to be done essentially by hand, and has not been performed for the current analysis, but it could benefit the accuracy of the $S(t)$ function and also recover some statistics in cases where the individual runs might be too short for inclusion in the lightmap dataset.

The choice of binning or parametrization for $R(\vec{x})$ and $S(t)$ can have a profound impact on the accuracy of the lightmap, and the current analysis has only skimmed the surface in trying options. It is hoped that further work on the lightmap will include significant investigation in these topics.

5.2.3 Convergence and Error Estimation

Our treatment of the convergence of algorithm 2 and the resulting statistical errors in $L(\vec{x}, t)$ is extremely rudimentary. Broadly convergence is checked not by analysis of the lightmap itself, but by verifying that the energy resolution from denoising is not improved by further iterations through algorithm 2. Lightmap errors do not directly enter into the calculations of denoising (which treats the lightmap as perfectly known), so they are not estimated at all in the current analysis.

As a proxy for estimation of the statistical errors in the lightmap, we instead study the number of hits observed in each position voxel of the detector (see section 5.4), and presume that the most significant source of error comes from low-statistics regions of the detector. This information can motivate future data-taking campaigns to probe the light response in those regions of the detector and reduce these uncertainties. However, no explicit estimation of the lightmap uncertainty has been attempted.

One difficulty with estimating the errors in the lightmap function $L(\vec{x}, t)$ comes from the correlation between errors in $R(\vec{x})$ and $S(t)$. If one of those two components were known perfectly, then we could treat the fit uncertainties of each hit as

independent errors, and propagate those errors into an uncertainty for each voxel of $R(\vec{x})$ (if $S(t)$ is assumed to be perfectly known) or $S(t)$ (if $R(\vec{x})$ is assumed to be perfectly known). But in reality, all of the measurements of $R(\vec{x})$ are correlated with all of the measurements of $S(t)$, meaning that even the errors of different voxels of $R(\vec{x})$ or different times in $S(t)$ are correlated with each other. Fully characterizing these errors could evolve into a significant project in itself, and it is not clear that the payoff could justify such an investment of effort or computation.

Although a full estimate of lightmap errors with correlations would probably be computationally quite intensive to produce, it might be possible to estimate the independent errors of each voxel of the position lightmap $R(\vec{x})$ or each independent run making up $S(t)$ by treating the other function as perfectly known, as described above. This would generally produce an underestimate of the uncertainty in each, but the estimate might still give some benefit.

To produce a more accurate estimate of errors, it would probably be necessary to do a simultaneous fit by varying both $R(\vec{x})$ and $S(t)$ together. In the current scheme, $R(\vec{x})$ contains far more complexity than $S(t)$ with roughly $50,000$ non-empty voxels, so for each APD gang we would need to simultaneously vary roughly $50,000$ parameters to obtain the optimal lightmap. It is exactly this time-intensive process which was avoided by choosing the iterative approach for measuring the lightmap; however, it would only need to be performed occasionally when deriving a new lightmap, so it is not infeasible to imagine attempting this project. The prospect of feeding in a high-quality guess obtained from the iterative method presents an additional significant time-saver. This method would not fully account for the cor-

relations between errors of the different voxels of $R(\vec{x})$ or runs in $S(t)$, but it would come closer than the naive method described earlier.

However, it is also possible that identifying the error of each voxel or run is heading down the wrong path. As described earlier, it is likely that the optimal (lowest-error) method for estimating the lightmap will be an unbinned method such as a locally-adaptive kernel regression method. Error estimation in kernel regression presents significant additional challenges compared to errors from binned parametrizations. At present, I am not aware of any simple scheme to manage this difficulty, meaning that there may be a paradoxical tradeoff that using the best method for minimizing lightmap errors simultaneously makes those errors infeasible to estimate.

Note that under the iterative method, the most naive method for estimating errors is not valid. It might appear that when $S(t)$ is initialized to a constant value of 1, we could also assign to it some constant error. Then when we compute $R(\vec{x})$, we could propagate independent errors from the fit uncertainties of signals and from $S(t)$; and when we compute $S(t)$ we could propagate independent errors from the fit uncertainties and from $R(\vec{x})$; and so forth. However, such a scheme provides no compensating feedback mechanism to force the iterated errors to a reasonable or accurate value, so there is no reason to believe the errors from such a system (if, that is, they converge at all). This difficulty may underscore the fundamental challenge associated with measuring the lightmap errors within our scheme – iterative methods are well-suited to solving a system, but when correlated errors are mistreated as uncorrelated an iterative method can easily magnify the

impact of that mistreatment.

On the topic of convergence, it has been mentioned already that by starting with a generally accurate initial guess for $S(t)$ as constant, the iterative solution method tends to converge rapidly. As a result, and because iterations take only a few hours to perform on a single machine, we currently perform three iterations and claim that convergence is approximately reached. Ideally, we would require that none of the position voxels or runs change value within an iteration by more than some fraction of their estimated errors; but in the absence of estimated errors, this is of course impossible.

It would be possible, in a conservative approach, to require each value to converge to some small fraction of an ADC unit, ensuring that the convergence is better than our ability to measure signals. Such a requirement might force us to compute more iterations than are truly warranted by our lightmap errors, but given the reasonable speed of each iteration, such a method still might not be unreasonable.

5.3 Implementation for this Analysis

The physics analysis which will be described in this paper includes data from EXO runs 2464 to 5597, which were taken between October 5, 2011 and September 1, 2013. However, at the time when the initial denoising processing was begun, the tentative range of runs to be used only extended up to 5367 on June 24, 2013. As a result, calibrated data at that point was only available up to June 24, 2013, and the lightmap had only been generated using the same set of Thorium source data.

When the run range for the present analysis was extended, a significant portion of the dataset had already been denoised with the lightmap based only on data extending to June 24, 2013. Although the possibility of creating a new lightmap was considered, this would have required a re-analysis and re-verification of the existing denoised dataset. As a result, the existing lightmap continued to be used. The functions $S(t)$, which had only been directly measured up to June 24, 2013, were assumed to remain constant between June 24 and September 1, 2013; no known changes to the APDs occurred during this time, nor did any known environmental factors change, so this assumption was considered acceptable. Future lightmaps of course will make use of a more complete dataset rather than relying on extrapolation.

Furthermore, one bug was discovered in the lightmap which was used for denoising. A set of Radium-226 source data was taken before the corresponding identifier could be set in data files, and as a result they were provisionally labeled as Thorium runs. These runs were mistakenly incorporated into the generated lightmap, and events from the 2204-keV gamma line of the Bismuth-214 daughter product of Radium-226 were selected and handled as though they were legitimate 2615-keV events.

It was possible to partially remedy this after the fact: since currently there is a one-to-one relationship between individual source runs and their corresponding points in the functions $S(t)$, it was possible to artificially erase the data points of $S(t)$ originating from Radium runs. It is not so easy to remove the impact they may have had on $R(\vec{x})$. However, the Radium runs were taken at a location which is extremely well-populated by Thorium data throughout the life of the detector; since
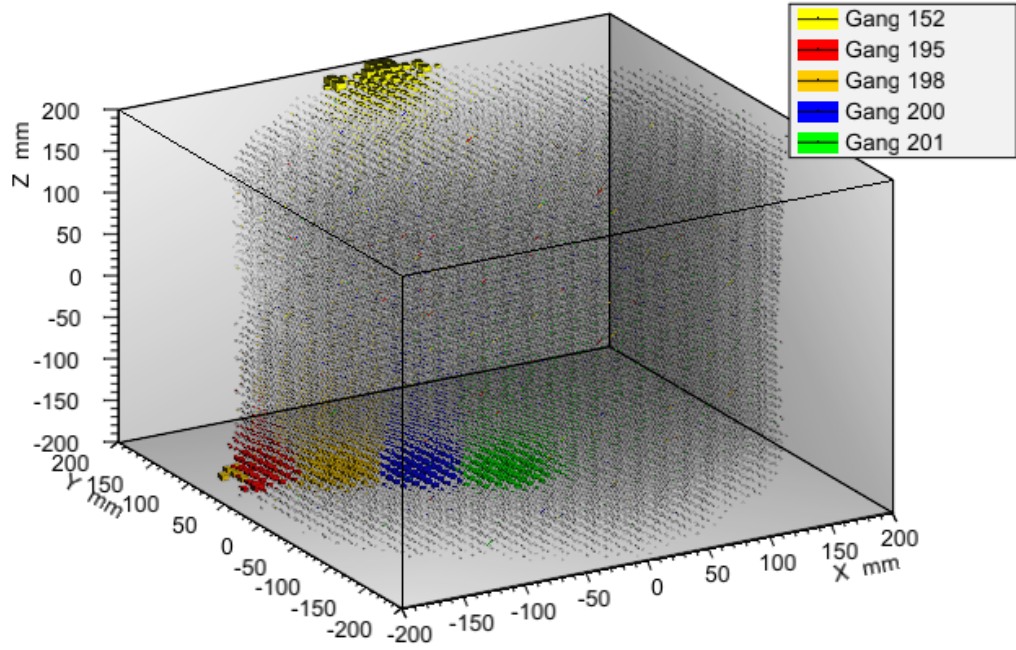
Figure 5.1: Lightmap position-dependence $R(\vec{x})$ for selected APD gangs.

the quantity of Radium data is small by comparison, the effect on $R(\vec{x})$ is presumed to be quite small. Subsequent studies using a correctly-generated lightmap on small subsets of data indicate that the effect is indeed negligible, as expected.

5.4 Visualization

Although it is not strictly necessary to be able to visually inspect the lightmap for it to be useful, nevertheless it is reassuring to see that the lightmap is qualitatively similar to intuitive expectations of how light should propagate through the detector. We have chosen to store the position-dependent $R(\vec{x})$ for each APD gang as a set
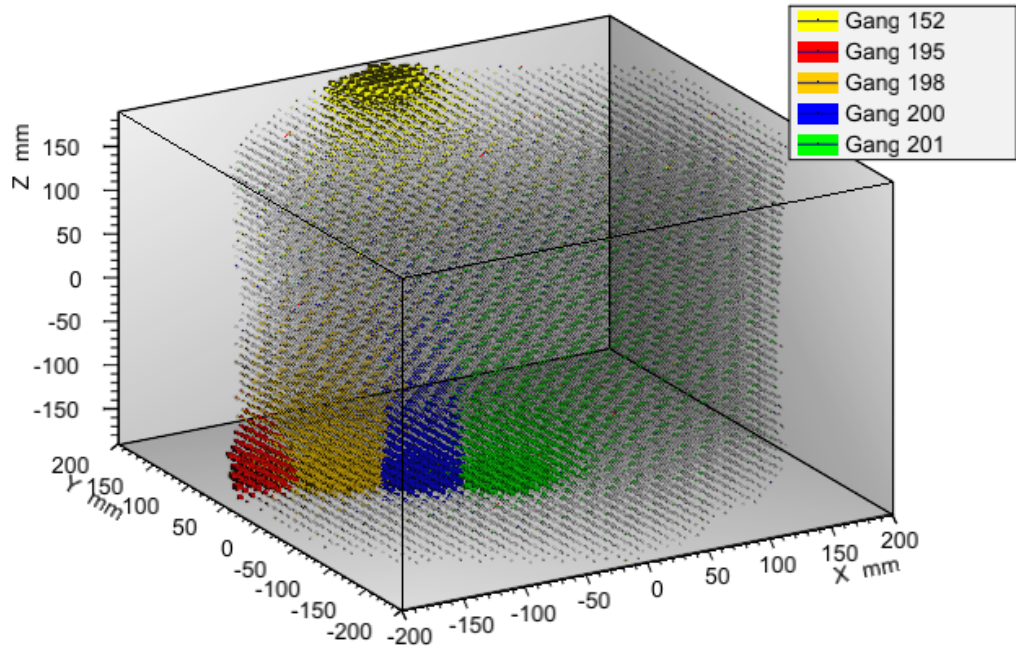
Figure 5.2: Lightmap position-dependence $R(\vec{x})$ for selected APD gangs. Here extreme anode positions are omitted to permit better contrast for the lightmap in the fiducial volume.
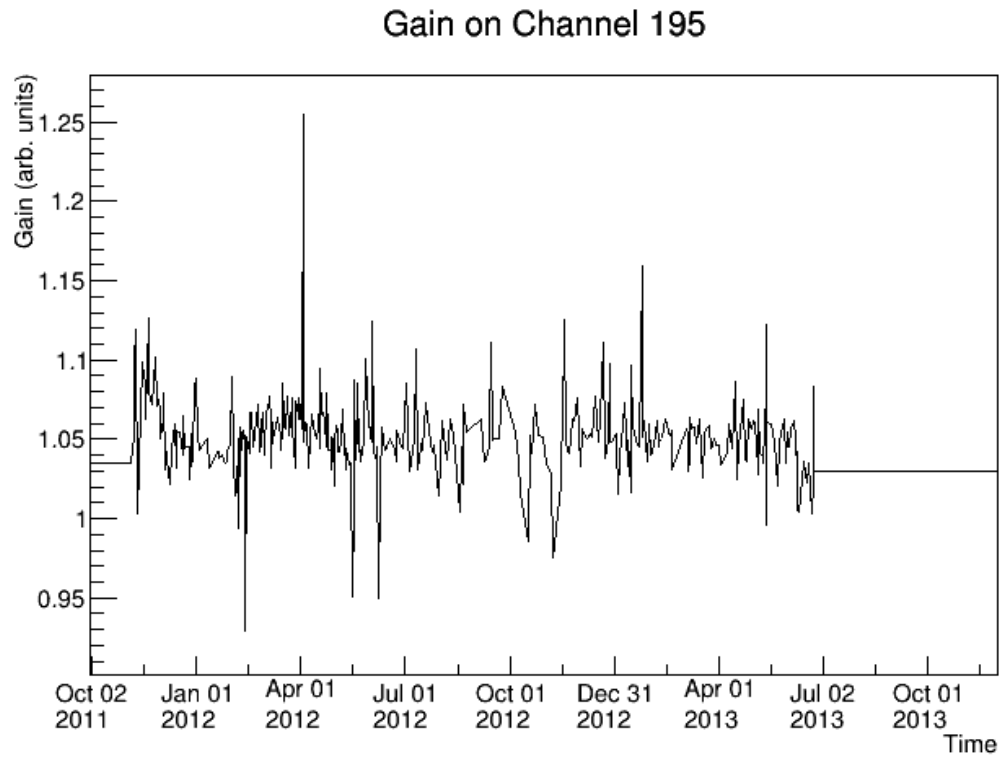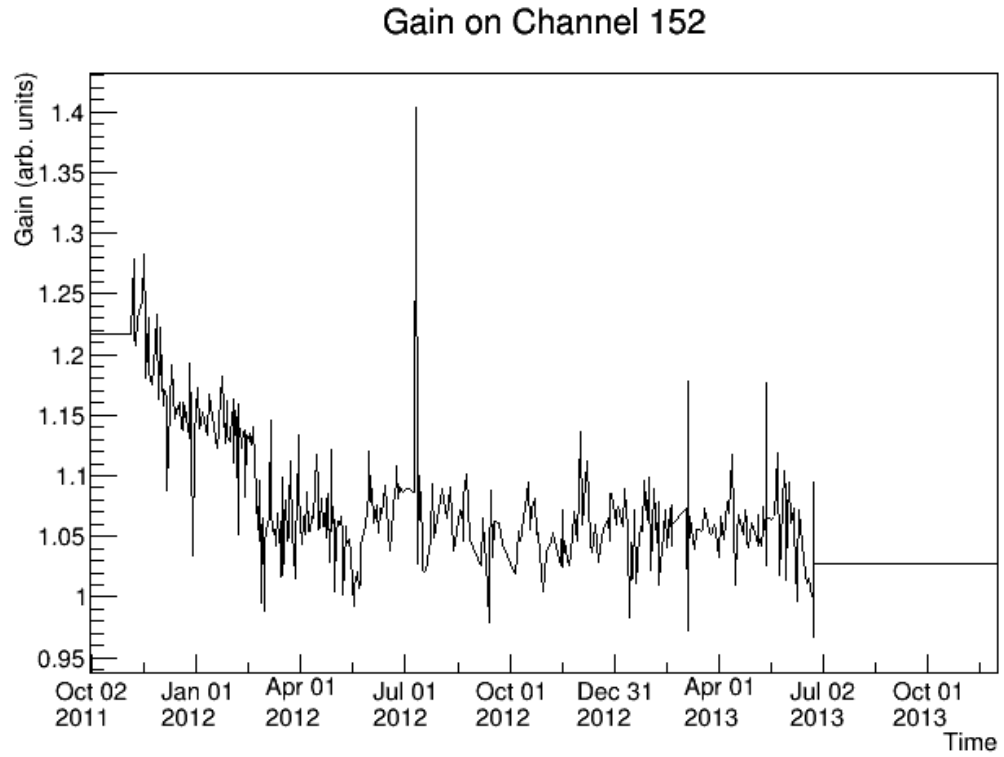
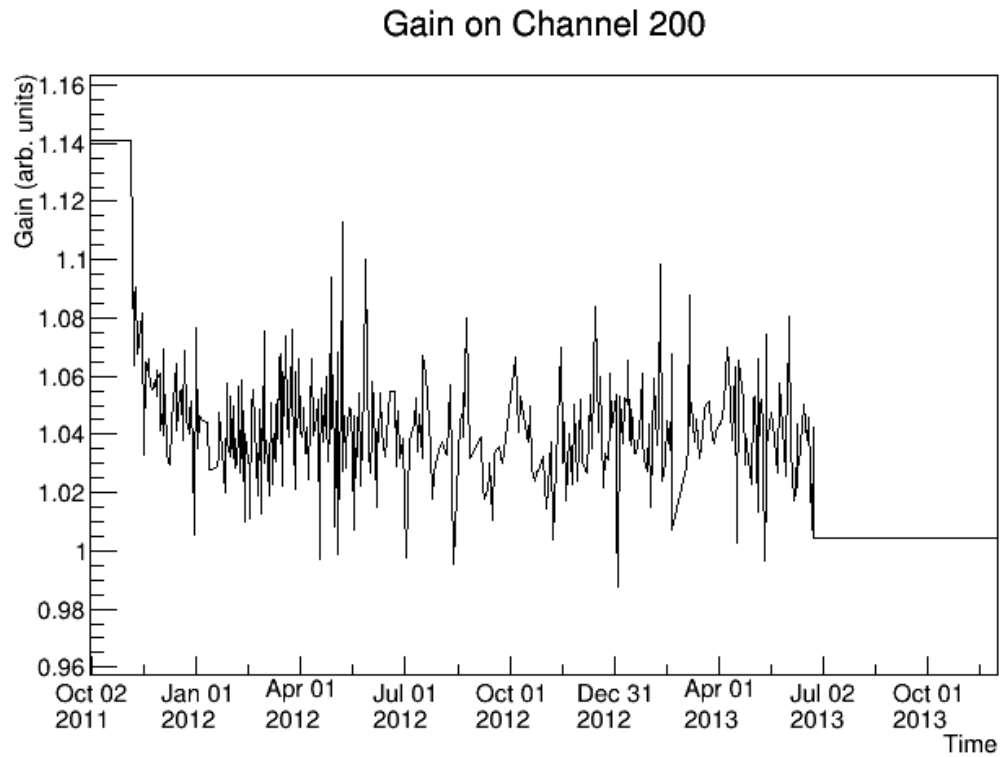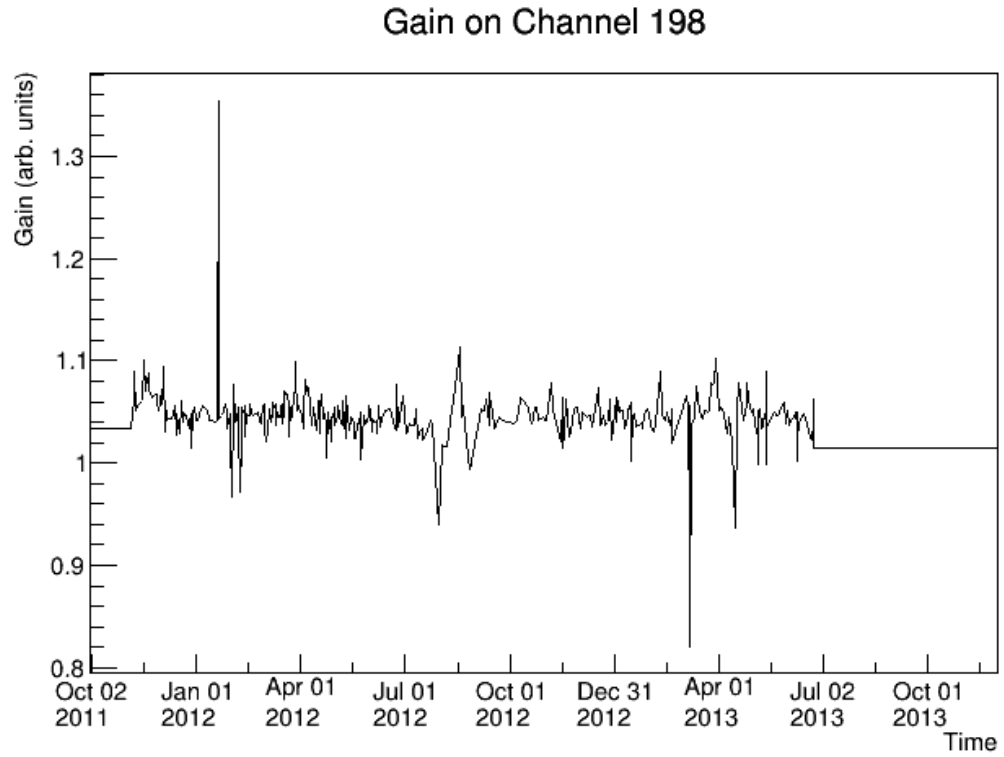Figure 5.3: Functions $S(t)$ for selected channels.

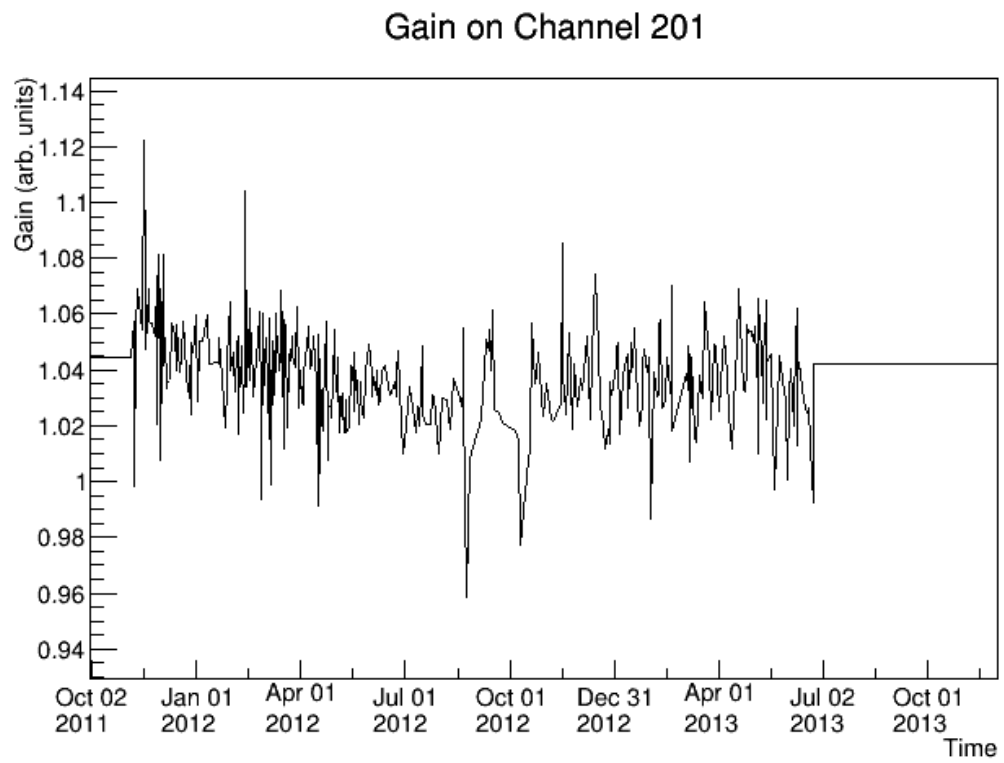Figure 5.4: Functions $S(t)$ for selected channels.

Figure 5.5: Functions $S(t)$ for selected channels.

of ROOT TH3D objects, and fortunately ROOT provides a number of excellent plotting features suitable for a three-dimensional dataset. In figure 5.1, it is possible to view the values of $R(\vec{x})$ for a sample of gangs on top of each other. Larger boxes and denser color indicates a higher yield on the APD gang in question, and it is immediately apparent that events near the anodes produce light which is highly concentrated on a single APD gang.

Figure 5.1 shows the highest yield on the very boundary of the detector, well outside of our fiducial volume; to permit us to more easily view contrast inside of the detector, figure 5.2 shows the same map while omitting the most extreme bin near either anode. Viewing this map, we can see more interesting characteristics of the lightmap:

- Events near the anodes show a high signal concentration on the one gang nearest to their position; however, even deep into the detector near the cathode it is still possible to see the higher concentration of signal on the gang directly aligned with the event.

- We can also see, from gang 201 (green) in this visualization, that events can produce significant signal on APD gangs which which they are not directly aligned (in the Z direction); yield on gang 201 can be seen to decrease smoothly in all directions.

- APD gangs in the corners of the detector, such as gang 195 (red), are not effective at measuring light from events which are far away; even directly above gang 195, it is clear that gang 198 is more effective at collecting light

farther away than about five to ten centimeters. This can be attributed to the reflection of photons by teflon, which may enhance the light yield on gangs which are not hidden in corners.

Figures 5.3, 5.4, and 5.5 show the functions $S(t)$ for the same sample of gangs. The vertical scale can be treated as having arbitrary units; we note that all of these functions lie roughly around 1, which is attributed to the initial placement of $S(t) = 1$ in algorithm 2. We draw the following primary observations from these plots:

- Many of the gangs show their values of $S(t)$ decreasing rapidly up to around February 2012; some of the gangs also show a sharp decrease in value at that point. The decrease in gain corresponds with observations which were made at the time, leading to a decision to replace electronics on some APD channels on February 23, 2012. Thus, we do see "real" features from these plots.

- The functions $S(t)$ are otherwise dominated by jitter between points, indicating that we do not collect enough statistics from each run to sufficiently constrain $S(t)$. This is taken as the strongest evidence that we should use a coarser time binning for $S(t)$, as described in section 5.2.2. Preliminary work has been performed to do this with more recent lightmaps, but no studies have evaluated the impact on energy resolution.

- Individual points on these functions may spike by as much as 40%. These points have been investigated, and their cause is not understood. These jumps,

along with the overall jitter, will certainly be reduced by the use of a coarser

time binning.

Chapter 5: Denoising Results

Bibliography

[1] F. T. Avignone, III, S. R. Elliott, and J. Engel. Double beta decay, majorana neutrinos, and neutrino mass. *Reviews in Modern Physics*, 80:481, 2008.

[2] A. S. Barabash. Double beta decay: present status. *Phys.Atom.Nucl.*, 73:162, 2010.

[3] L. S. Blackford, J. Demmel, J. Dongarra, I. Duff, S. Hammarling, G. Henry, M. Heroux, L. Kaufman, A. Lumsdaine, A. Petitet, R. Pozo, K. Remington, and R. C. Whaley. An updated set of basic linear algebra subprograms (blas). *ACM Trans. Math. Soft.*, 28(2):135, 2002.

[4] J. Wolf (KATRIN Collaboration). The KATRIN neutrino mass experiment. *Nuclear Instruments and Methods in Physics Research A*, 623:442, 2010.

[5] Planck Collaboration. Planck 2013 results. xvi. cosmological parameters. *Astronomy and Astrophysics*, under review.

[6] SINDRUM II Collaboration. Improved limit on the branching ratio of $\mu \to e^+$ conversion on titanium. *Physics Letters B*, 422:334–338, 1998.

[7] Arthur H. Compton. A quantum theory of the scattering of x-rays by light elements. *Physical Review*, 21:483, 1923.

[8] D.S. Leonard et al. Systematic study of trace radioactive impurities in candidate construction materials for EXO-200. *Nucl. Instrum. Meth. A*, 591:490, 2008.

[9] H. V. Klapdor-Kleingrothaus et al. Latest results from the heidelberg-moscow double beta decay experiment. *Eur. Phys. J. A*, 12:147, 2001.

[10] R. Neilson et al. Characterization of large area apds for the EXO-200 detector. *Nucl. Instrum. Meth. A*, 608:68, 2009.

[11] Szydagis et al. NEST: A comprehensive model for scintillation yield in liquid xenon. *JINST*, 6:P10002, 2011.

[12] V. M. Lobashev et al. Direct search for mass of neutrino and anomaly in the tritium beta-spectrum. *Physics Letters B*, 460:227–235, 1999.

[13] K. Nakamura et al. (Particle Data Group). Something from pdg. *J. Phys. G*, 37:075021, 2010.

[14] H. Nishino et al. (Super-Kamiokande Collaboration). Search for proton decay via $p \rightarrow e + \pi 0$ and $p \rightarrow \mu + \pi 0$ in a large water cherenkov detector. *Phys. Rev. Lett.*, 102:141801, 2009.

[15] Y. Fukuda et al. (Super-Kamiokande Collaboration). Evidence for oscillation of atmospheric neutrinos. *Phys. Rev. Lett.*, 81:15621567, 1998.

[16] G. Feinberg, P. Kabir, and S. Weinberg. Transformation of muons into electrons. *Phys. Rev. Lett.*, 3:527, 1959.

[17] Kazushige Goto and Robert A. van de Geijn. Anatomy of high-performance matrix multiplication. *ACM Trans. Math. Softw.*, 34(3):12:1–12:25, May 2008.

[18] A. El Guennouni, K. Jbilou, and H. Sadok. A block version of BiCGSTAB for linear systems with multiple right-hand sides. *Electronic Transactions on Numerical Analysis*, 16:129, 2003.

[19] C. Hall. Status of the EXO double beta decay search. In *ICHEP 2010 Conference*, 2010.

[20] S. Herrin. *Double Beta Decay in Xenon-136: Measuring the Neutrino-Emitting Mode and Searching for Majoron-Emitting Modes.* PhD thesis, Stanford University, 2013.

[21] Intel. *Reference Manual for Intel Math Kernel Library*, 11.1 edition.

[22] H. V. Klapdor-Kleingrothaus and I. V. Krivosheina. Evidence for neutrinoless double beta decay. *Mod. Phys. Lett. A*, 21:20:1547, 2006.

[23] E. Majorana. Teoria simmetrica dellelettrone e del positrone. *Nuovo Cimento*, 14:171, 1937.

[24] Sheldon Ross. *A First Course in Probability*. Pearson Prentice Hall, 2006.

[25] J. Schechter and J.W.F. Valle. Neutrinoless double-β decay in su(2)×u(1) theories. *Phys. Rev. D*, 25:2951, 1982.

[26] David W. Scott. *Multivariate density estimation : theory, practice, and visualization.* 1992.

[27] L. Yang. EXO-200 electronics upgrade study report. Internal Document, 2013.